Electronic Supplementary Material (ESI) for Journal of Materials Chemistry A.

Dynamic {Au^I…Au^I}-Coupling Cluster-Based Coordination Capsule for Photocatalytic Benzylamine Oxidation

Ping Shang, [a] Yu-Hua Li, [a] Xing-Yu Chen, [a] Yu-Qing Xiao, [a] Xiao-Qian Pu, [a] Kai-Wen Jiang, [a] Xuan-Feng Jiang [a, b, c] *

[a] Key Laboratory of Green Preparation and Application for Functional Materials, Ministry of Education, Hubei Key Laboratory of Polymer Science, School of Materials Science and Engineering, Hubei University, Wuhan, Hubei, 430062, P. R. China.

E-mail: xuanfengjiang@hubu.edu.cn

[b] Hubei Jiangxia Laboratory, 430200, Wuhan, China.

[c] Hubei Key Laboratory of Processing and Application of Catalytic Materials, Huanggang Normal University, Huanggang, Hubei, 438000, P. R. China.

Table of Contents

S1. Materials and Instrumentation

All the organic solvents were obtained from commercial chemical company and used here were distilled over 4 Å molecular sieves under an argon atmosphere. All other chemicals were used as received without any further purification. NMR spectra were recorded on Bruker AVIII 500 MHz and 400 MHz spectrometers and referenced to residual solvent peaks. The working frequencies were 500 MHz or 400 MHz for ^1H, 101 MHz for ^{13}C and 162 MHz for $^{31}P\{^1H\}$. The ESI-MS spectral analyses were carried out on a Q Exactive Thermo Scientific spectrometer. Fourier transform infrared (FT-IR) spectra were collected on a Thermo Nicolet FTIR-IS50 spectrometer. The samples were ground with spectrographically KBr and tableted as a transparent slice. X-ray photoelectron spectroscopy (XPS) was performed on a Thermo Scientific Escalab 250Xi photoelectron spectrometer. The X-ray diffraction single-crystal data of the dimeric capsule $[\mathbf{C1}]_2 \bullet 6PF_6^-$ was collected on a Bruker D8 Venture APEX II CCD single crystal diffractometer. Powder X-ray Diffraction (PXRD) data were collected on a Bruker D8 Advance powder X-ray diffractometer. The UV-Vis absorption spectral analyses were carried out on a UV-3600 spectrometer. Fluorescence spectral analyses were performed on a Tianjin Gangdong F-320 spectrometer and an Edinburgh FLS980. The electron paramagnetic resonance spectroscopy (EPR) measurements of organic radicals were carried out on a Bruker EMXplus spectrometer (10 dB; 9.5 GHz). Mott-Schottky plot, photocurrent responses and electrochemical impedance spectroscopy were conducted at the CHI 660A electrochemical workstation. Scanning electron microscopy (SEM) and energy dispersive spectrometer (EDS) were acquired on an OPTON SIGMA500 field emission scanning electron microscope.

S2. Synthesis and Characterization of All Compounds

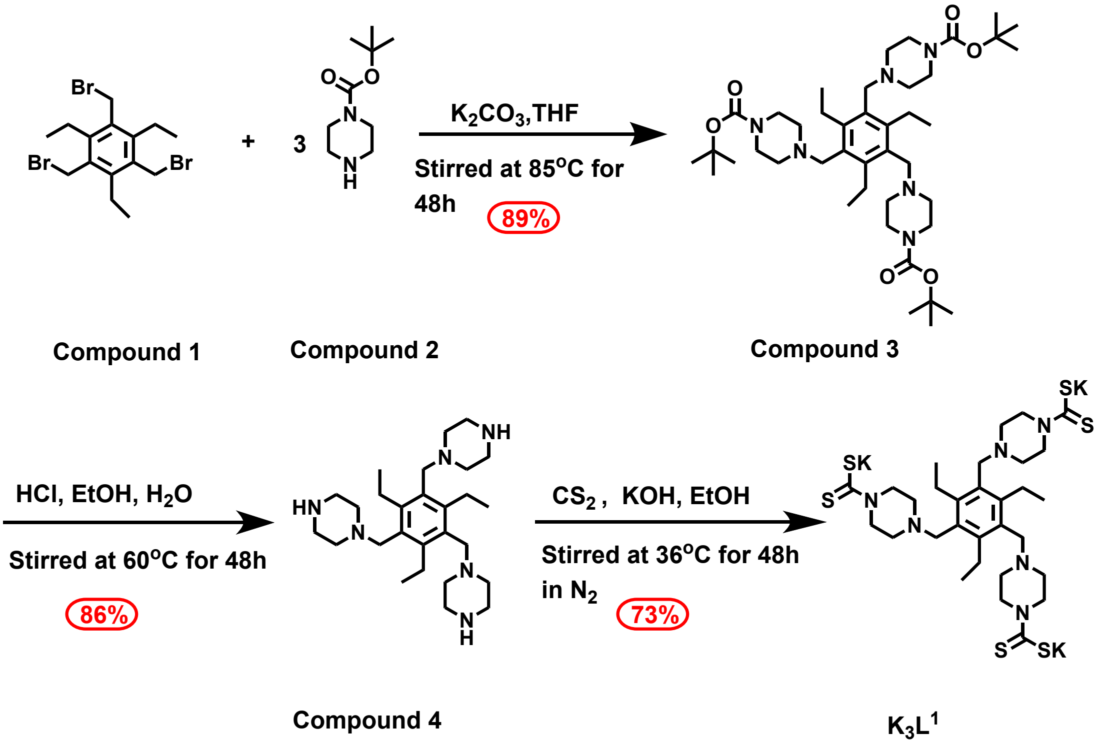

Scheme S1. Synthetic routes of the tripodal ligand **K_3L^1**.

Synthesis of 1, 3, 5-tri (1-Boc-4-piperazinyl)-2, 4, 6-triethylbenzene (compound 3)

1,3,5-Tris(bromomethyl)-2,4,6-triethyl benzene (2 g, 4.57 mmol), 1-piperazine-Boc (2.58 g, 13.9 mmol) and potassium carbonate (3.15 g, 22.83 mmol) were refluxed in THF (80 mL) at 85 °C for about 48 h. After the removal of organic solvents, the residue was washed with water and extracted with dichloromethane for three times. The dichloromethane extracts were dried over anhydrous Na_2SO_4 and the solvent was distilled under vacuum. Chromatography on silica gel elution with dichloromethane/methanol (v/v, 6:1) afforded the pure product 1, 3, 5-tri (1-Boc-4-piperazinyl)-2, 4, 6-triethylbenzene (compound **3**) as faint yellow powders (3.07 g, 4.05 mmol) in a yield of 89%. ^1H NMR (298K, 400 MHz, $CDCl_3$-*d*) $\delta = 3.52$ (s, 2H), 3.36 (s, 4H), 2.91-2.86 (q, $J = 7.3$ Hz, 2H), 2.41 (s, 4H), 1.45 (s, 9H), 1.13-1.10 (t, $J = 7.3$ Hz, 3H).

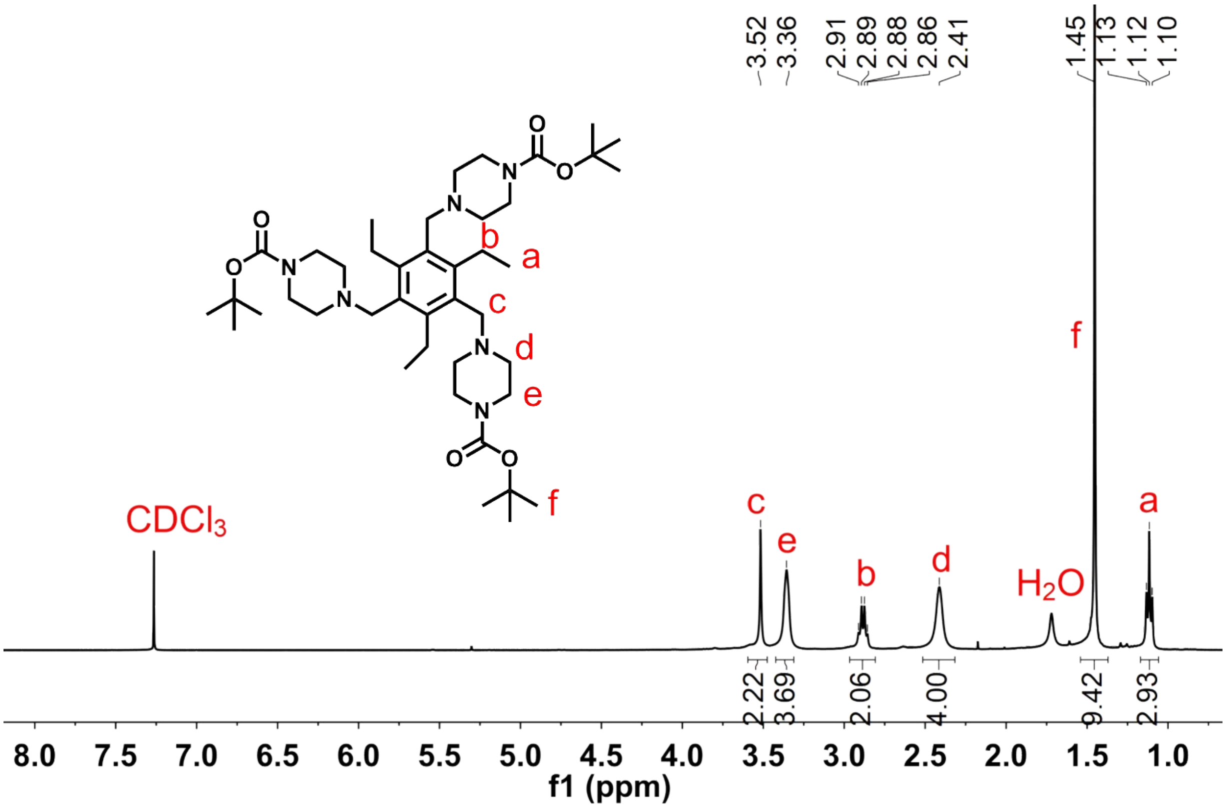

Figure S1. ^{1}H NMR spectrum (298 K, 400 MHz, $CDCl_3$-*d*) of compound **3**.

Synthesis of 1, 3, 5-tri (1- piperazinyl)-2, 4, 6-triethylbenzene (compound 4)

1, 3, 5-tri (1-Boc-4-piperazinyl)-2, 4, 6-triethylbenzene (3.0 g, 3.97 mmol), 1 mL of water and 15 mL of concentrated hydrochloric acid (1 M) were added into a flask and the reactants were refluxed in 20 mL of ethyl alcohol at 60 °C for 48 h. After the reaction mixture cooled to room temperature, the solvent was evaporated under reduced pressure and dissolved in distilled water, and then a concentrated NaOH solution was slowly added to the mixture and neutralizing the pH value to 14. Next, the mixture solution was washed and extracted with dichloromethane (50 mL × 3). The dichloromethane extracts were dried over anhydrous Na_2SO_4 and removed under vacuum. Compound **4** was obtained as yellow powders in a high yield (1.56 g, yield 86%). ^{1}H NMR (298K, 400 MHz, $CDCl_3$-*d*) δ = 3.48 (s, 2H), 2.93-2.88 (q, *J* = 7.4 Hz, 2H), 2.82-2.80 (t, *J* = 4.6 Hz, 4H), 2.45 (s, 4H), 1.14-1.10 (t, *J* = 7.4 Hz, 3H). ESI-MS (CH_3OH) m/z：[M+H]$^+$, calcd for $C_{27}H_{48}N_6^+$, 456.4；found, 457.6.

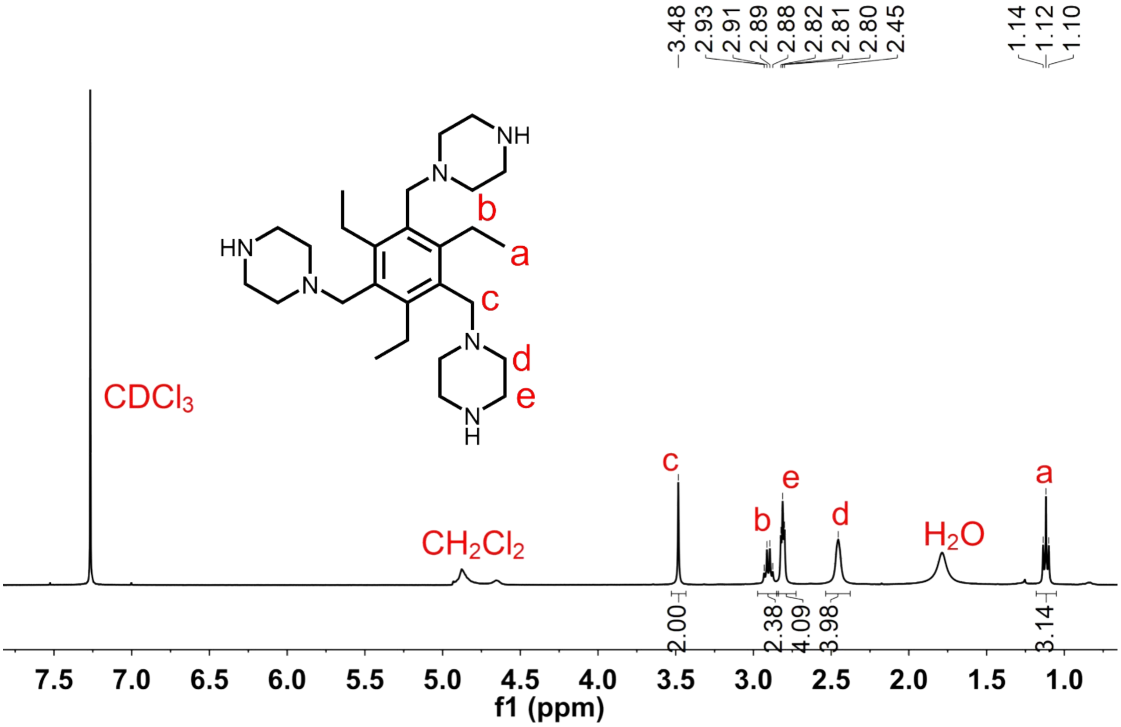

Figure S2. ^{1}H NMR spectrum (298 K, 400 MHz, $CDCl_3$-*d*) of compound **4**.

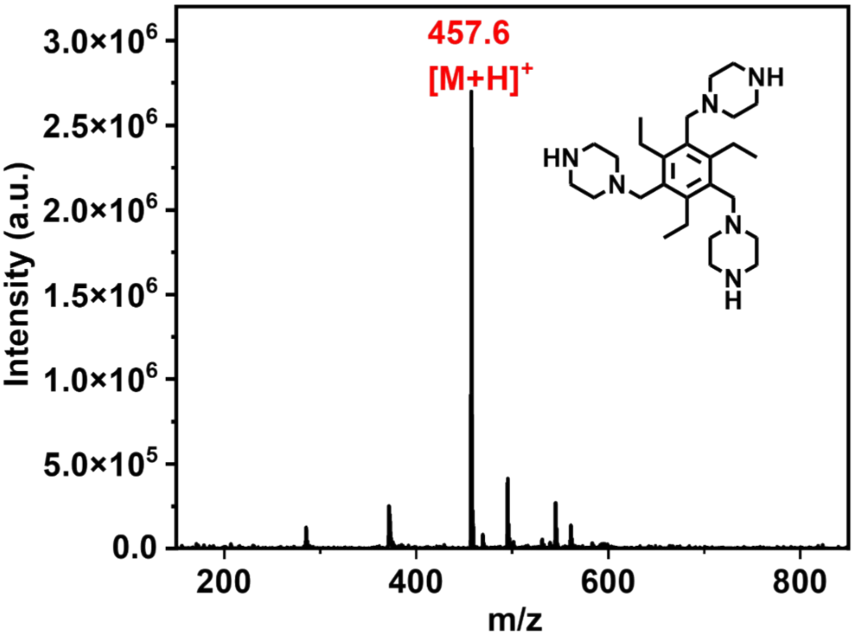

Figure S3. ESI-MS spectrum of compound **4** in CH_3OH at 298 K.

Synthesis of 1, 3, 5-tri (1- piperazinyl)-2, 4, 6-triethylbenzene potassium salt (K_3L^1)

1, 3, 5-tri (1-piperazinyl)-2, 4, 6-triethylbenzene (1.40 g, 3.07 mmol) and KOH (1.7 g, 30.7 mmol) were added to a mixed solution of CS_2 (150.0 mg, 4 mmol) in the mixed solution of water (5 mL) and methanol (10.0 mL). The mixture was stirred at 40 ºC under an argon atmosphere for 48 h. The solution was then cooled and concentrated. The white solid was filtered off, washed with acetone (20 mL) and dried under vacuum. Crystallization of the residue from CH_3OH/ diethyl ether (V/V, 1:1) afforded the target compound (yield: 1.79 g, 73%) as a white crystalline solid. ^{1}H NMR (298K, 400 MHz, DMSO-d_6) δ = 4.25-4.20 (q, J = 6.8 Hz, 4H), 3.47 (s, 2H), 2.89-2.85 (m, 2H), 2.34 (t, J = 5.0 Hz, 4H), 1.14-1.10 (t, J = 7.2 Hz, 3H). ^{13}C NMR (298K, 101 MHz, DMSO-d_6) δ = 214.42, 144.71, 144.35, 131.68, 131.54, 55.21, 53.02, 50.54, 49.79, 22.75, 16.86, 16.82.

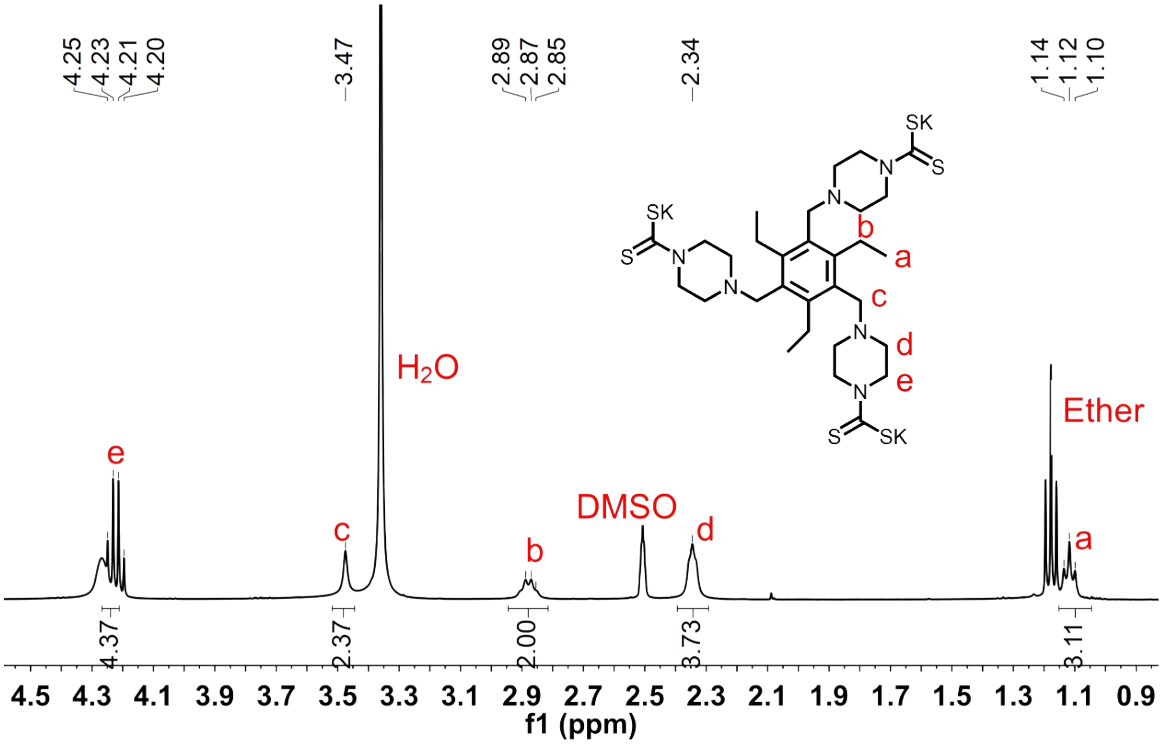

Figure S4. ^{1}H NMR spectrum (298 K, 400 MHz, DMSO-d_6) of the tripodal ligand **K_3L^1**.

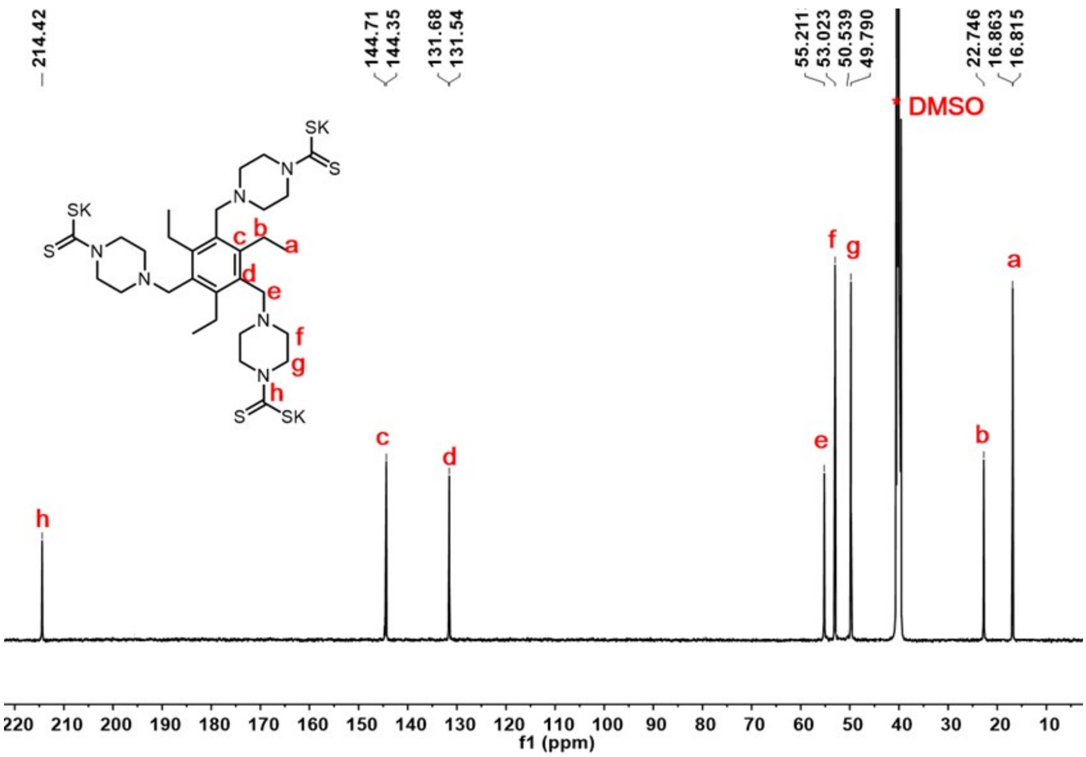

Figure S5. ^{13}C NMR spectrum (298 K, 101 MHz, DMSO-d_6) of the tripodal ligand **K_3L^1**.

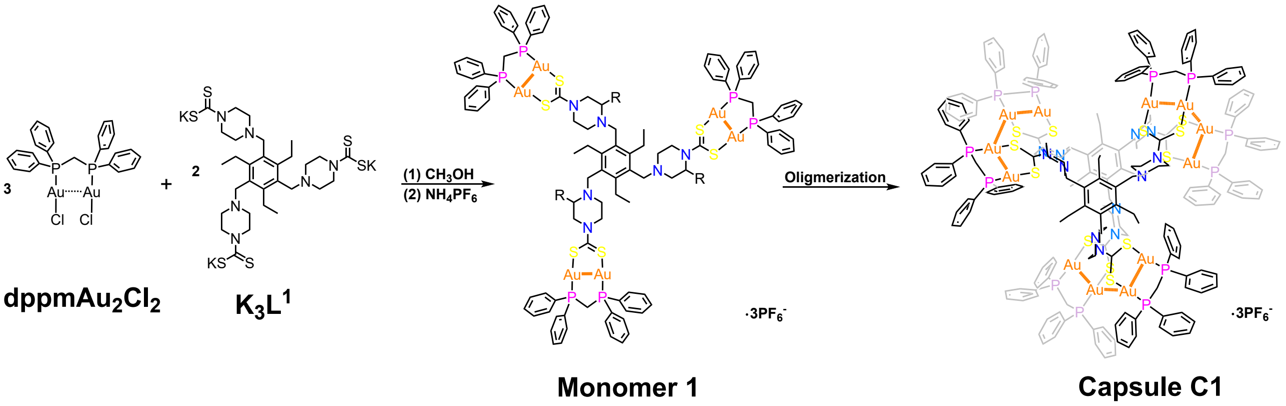

Scheme S2. Self-assembly pathway of the dimeric cluster-based capsule [**C1**]$_2$•6PF$_6^-$.

[**C1**]$_2$•6PF$_6^-$: A methanol solution of 1, 3, 5-tri(N-dithiocarbamates-1-piperazinyl)-2, 4, 6-triethylbenzene potassium salt **K_3L^1** (0.1 mmol) was slowly added to a suspension of binuclear corner dppmAu$_2$Cl$_2$ (0.3 mmol) in 3 mL methanol. The reaction was stirred for 24 hours until the mixture became a clear green-yellow solution at room temperature. Then the 10-fold excess of NH$_4$PF$_6$ was added to the resulting mixture solution, and the crude product [**C1**]$_2$•6PF$_6^-$ precipitated immediately as a yellow solid (yield of 85%). A single crystal of [**C1**]$_2$•6PF$_6^-$ was obtained by slow diffusion of diethyl ether into its 1:1 dichloromethane/methanol solution at a low temperature (3 °C) to give

[**C1**]$_2$•6PF_6^- as diffraction-quality yellow block crystals with a yield: 70%. ^{1}H NMR (298K, 400 MHz, DMSO-*d*$_6$) δ = 7.76-7.72 (m, 8H), 7.51-7.48 (t, *J* = 7.0 Hz, 4H), 7.42-7.39 (t, *J* = 7.2 Hz, 8H), 4.77-4.71 (t, *J* = 14.1 Hz, 2H), 4.27 (s, 3H), 3.66 (s, 2H), 2.96-2.95 (d, *J* = 7.3 Hz, 2H), 2.70 (s, 2H), 1.19-1.16 (m, 3H). ^{13}C NMR (298K, 101 MHz, DMSO-*d*$_6$) δ = 200.99, 133.67, 133.33, 132.76, 132.58, 129.62, 129.41, 56.55, 52.02, 49.07, 18.92, 16.90. ^{31}P NMR (298K, 162 MHz, DMSO-*d*$_6$) δ = 34.28, 29.36, 28.02, -135.41, -139.80, -144.18, -148.58, -152.97. IR (KBr, ν / cm^{-1}): ν (cm^{-1}) = 1627 (C=N), 1348 (C-N), 781 (C-P), 842 (PF_6^-), 689 (C-S). ESI-MS (CH_3CH_2OH/CH_2Cl_2) m/z：[**C1**+ OH^-+CH_2Cl_2]$^{2+}$, calcd for $C_{107}H_{114}Au_6N_6OP_6S_6Cl_2^{2+}$, 1559.16；found, 1559.14; [**C1**+ PF_6^-+CH_2Cl_2+CH_3CH_2OH+PF_6^-]$^{2+}$ calcd for $C_{108}H_{119}Au_6Cl_2F_6N_6OP_7S_6^{2+}$, 1647.16; found, 1647.05; [2**C1**+ 2PF_6^-+ OH^-+CH_3CN]$^{3+}$ calcd for $C_{212}H_{226}Au_{12}F_{12}N_7OP_{14}S_{12}^{3+}$, 2128.90; found, 2128.17; [2**C1**+ 3PF_6^-+ H_2O+CH_3CH_2OH]$^{3+}$ calcd for $C_{212}H_{226}Au_{12}F_{12}N_7OP_{14}S_{12}^{3+}$, 2177.56; found, 2176.82.

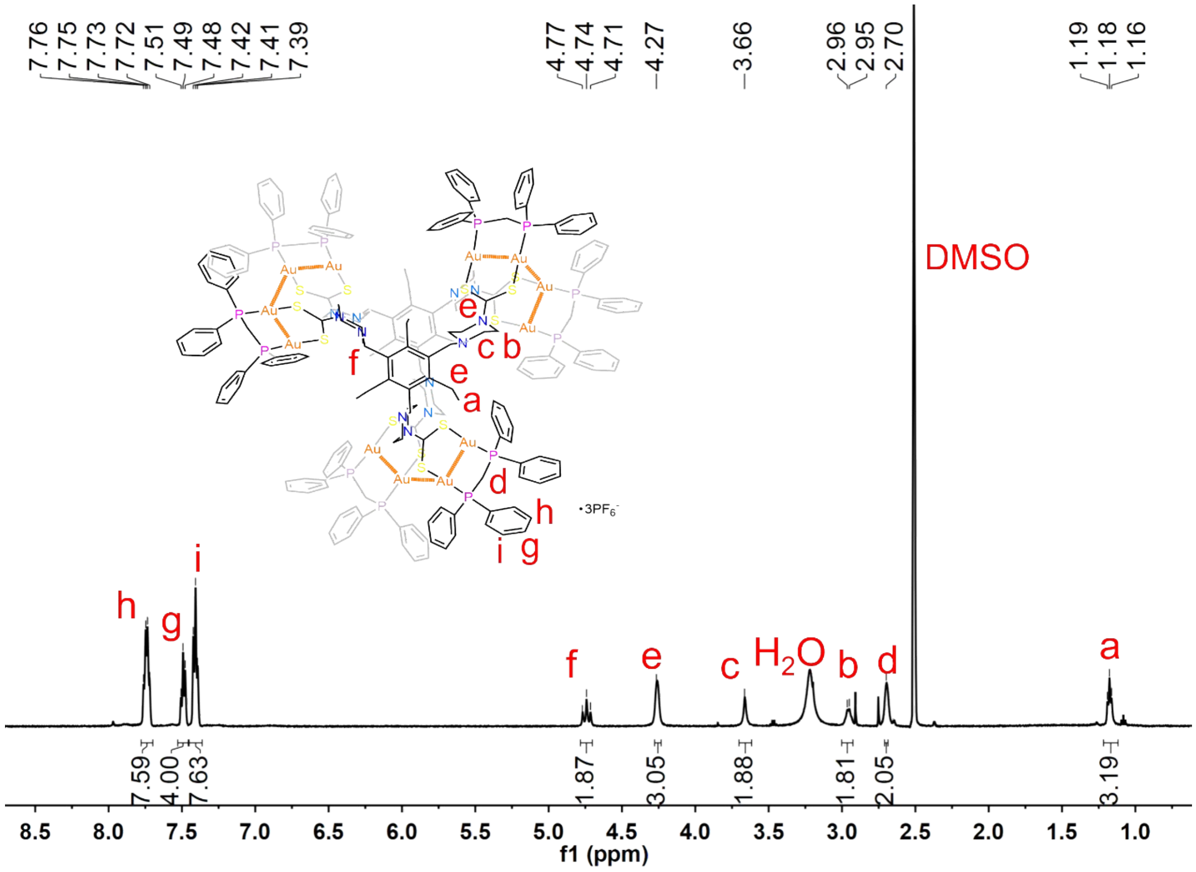

Figure S6. ^{1}H NMR spectrum (298 K, 400 MHz, DMSO-*d*$_6$) of cluster capsule [**C1**]$_2$•6PF_6^-.

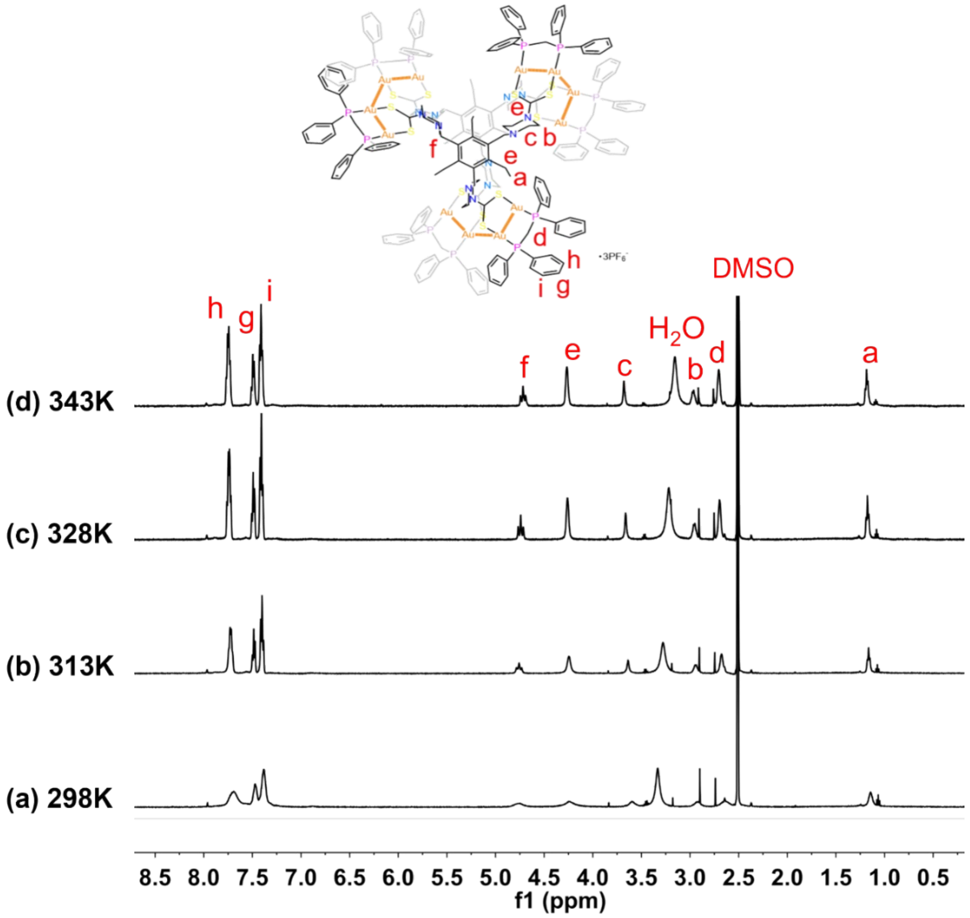

Figure S7. Variable temperature ^{1}H NMR spectroscopes (500 MHz, DMSO-d_6) of cluster capsule [**C1**]$_2$•6PF$_6^-$.

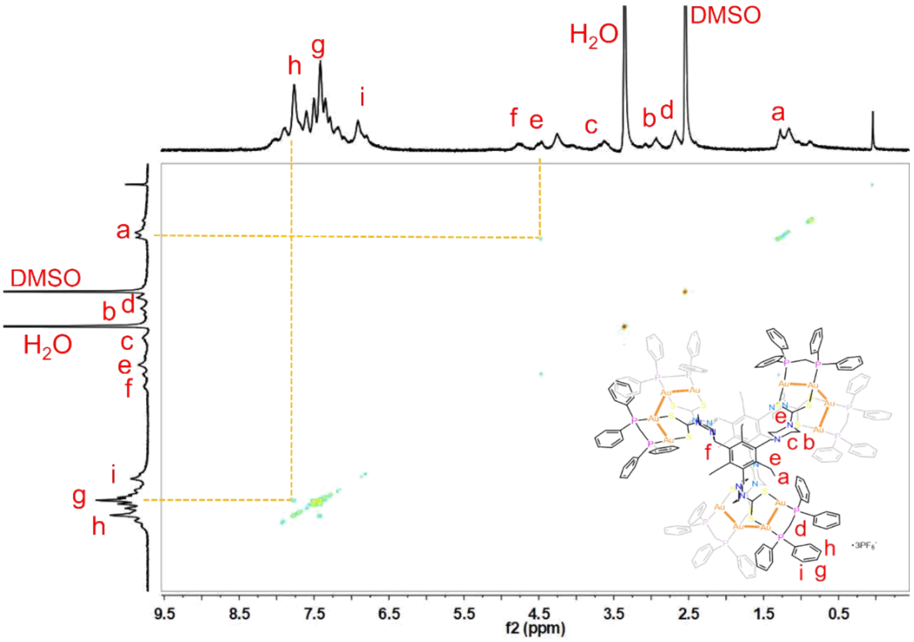

Figure S8. ^{1}H-^{1}H COSY NMR spectrum (298 K, 400 MHz, DMSO-d_6) of cluster capsule [**C1**]$_2$•6PF$_6^-$.

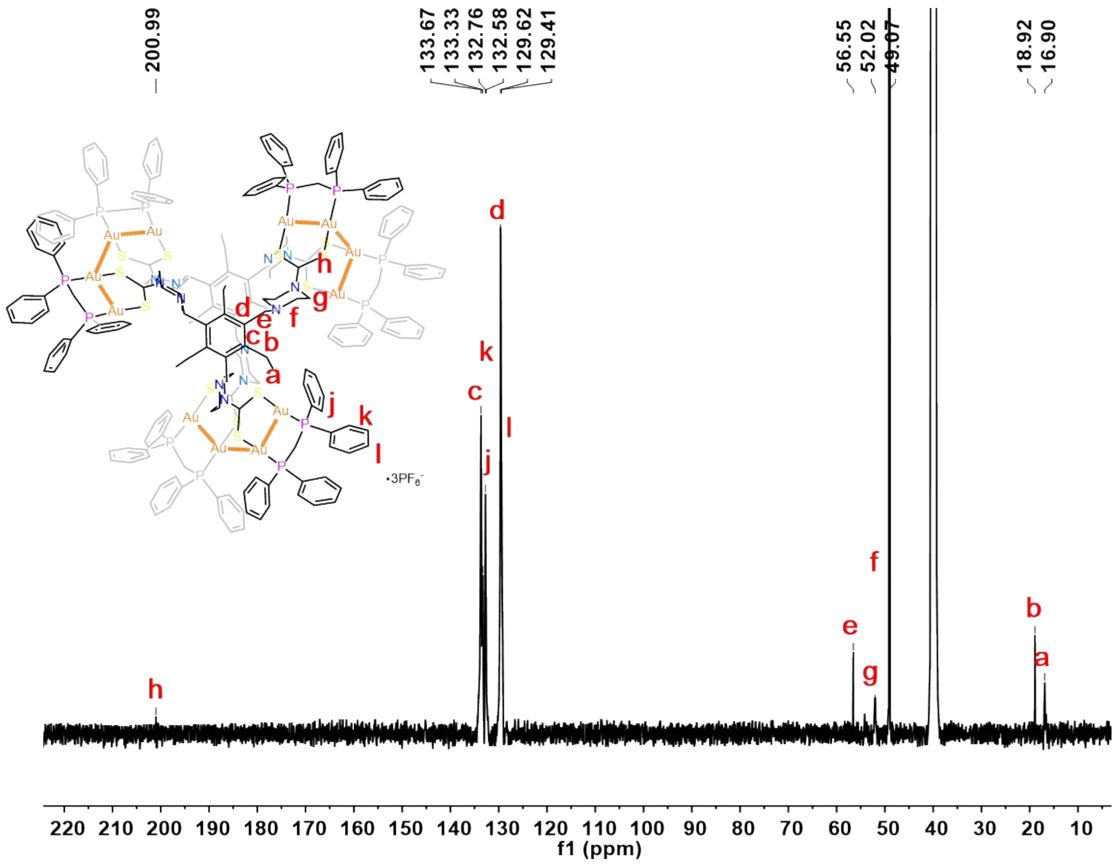

Figure S9. ^{13}C NMR spectrum (298 K, 101 MHz, DMSO-d_6) of cluster capsule [**C1**]$_2$•6PF$_6^-$.

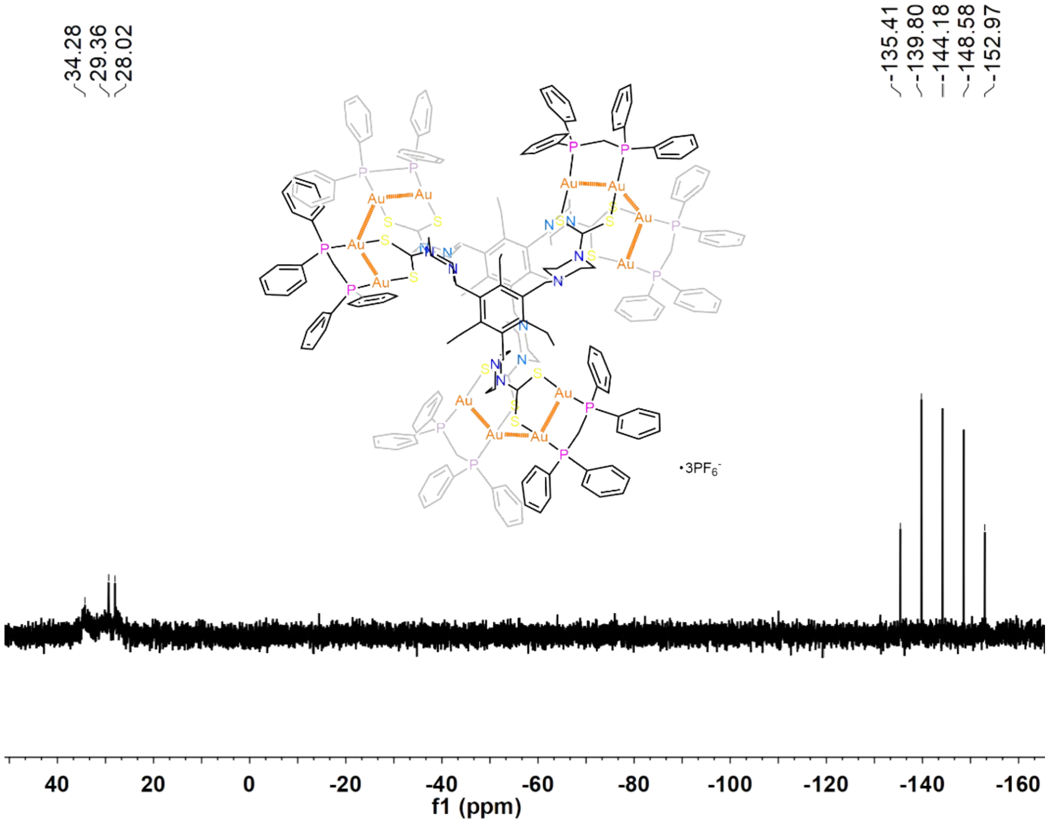

Figure S10. ^{31}P{^{1}H} NMR spectrum (298 K, 162 MHz, DMSO-d_6) of cluster capsule [**C1**]$_2$•6PF$_6^-$.

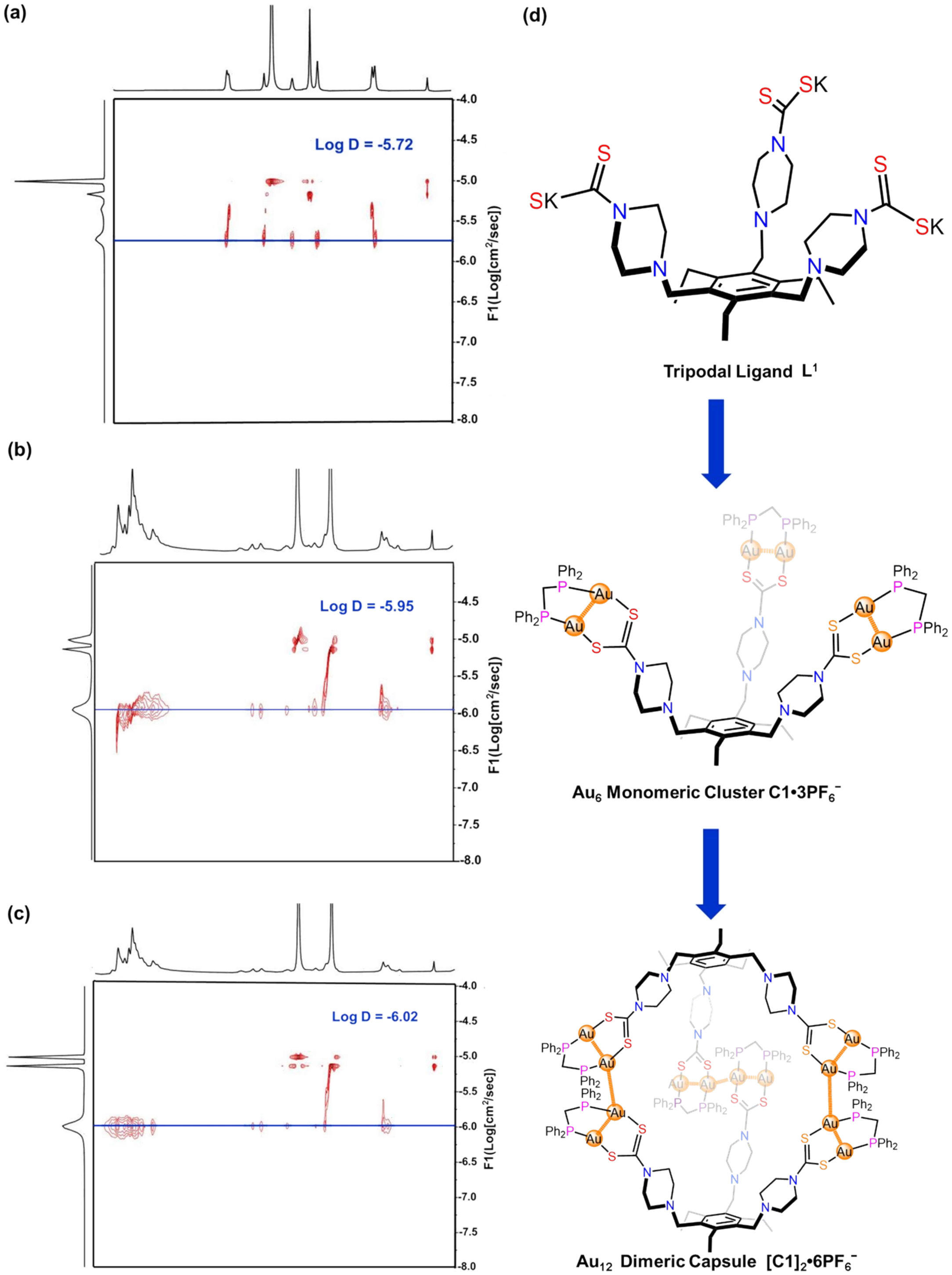

Figure S11. (a) DOSY NMR spectrum (298 K, 500 MHz, DMSO-*d₆*) of the free ligand **K$_3$L^1** (c = 5x10^{-3} M). (b) DOSY NMR spectrum (298 K, 500 MHz, DMSO-*d₆*) of cluster capsule [**C1**]$_2$•6PF$_6^-$ (c = 2.5x10^{-3} M). (c) DOSY NMR spectrum (298 K, 500 MHz, DMSO-*d₆*) of cluster capsule [**C1**]$_2$•6PF$_6^-$ (c = 5x10^{-3} M). (d) The proposed stepwise aggregation process of dimeric capsule [**C1**]$_2$•6PF$_6^-$ in solution.

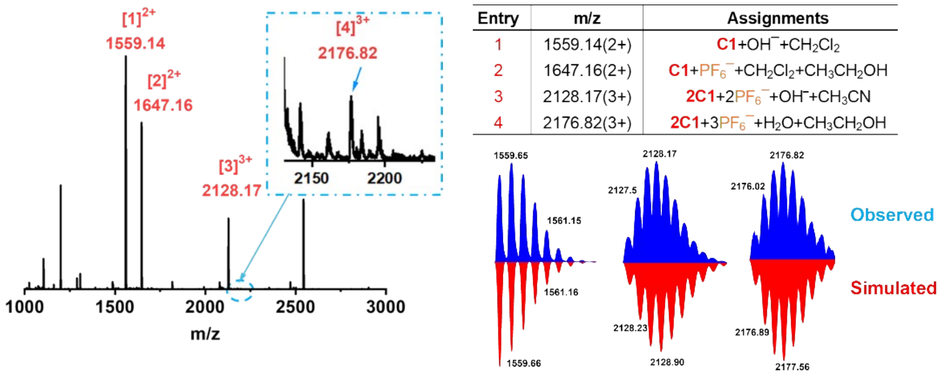

Entry	m/z	Assignments
1	1559.14(2+)	**C1**+OH^-+CH_2Cl_2
2	1647.16(2+)	**C1**+PF_6^-+CH_2Cl_2+CH_3CH_2OH
3	2128.17(3+)	**2C1**+2PF_6^-+OH^-+CH_3CN
4	2176.82(3+)	**2C1**+3PF_6^-+H_2O+CH_3CH_2OH

Figure S12. ESI-MS spectrum of cluster capsule [**C1**]$_2$•6PF_6^- in CH_3CH_2OH/CH_2Cl_2 mixture solution at 298 K. Insert shows observed isotope distribution patterns of two ionized peaks (m/z).

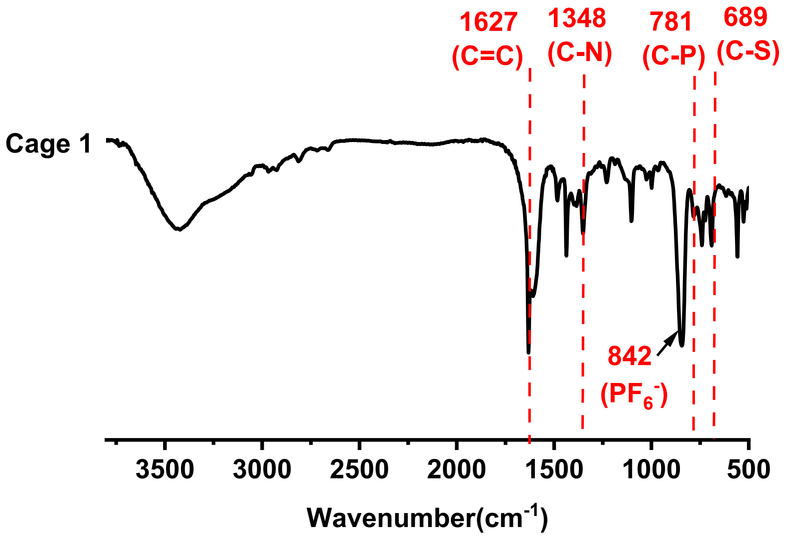

Figure S13. FT-IR spectra of cluster-based capsule [**C1**]$_2$•6PF_6^-.

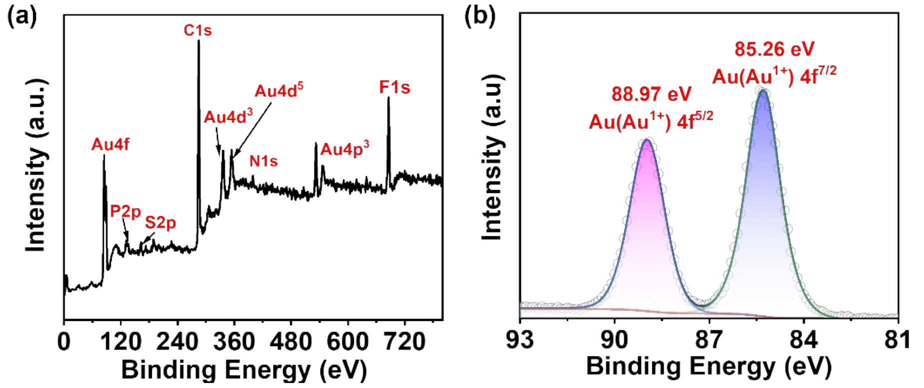

Figure S14. (a) The XPS profiles of capsule [**C1**]$_2$•6PF_6^-. (b) The narrow scan XPS spectra of ‘Au’.

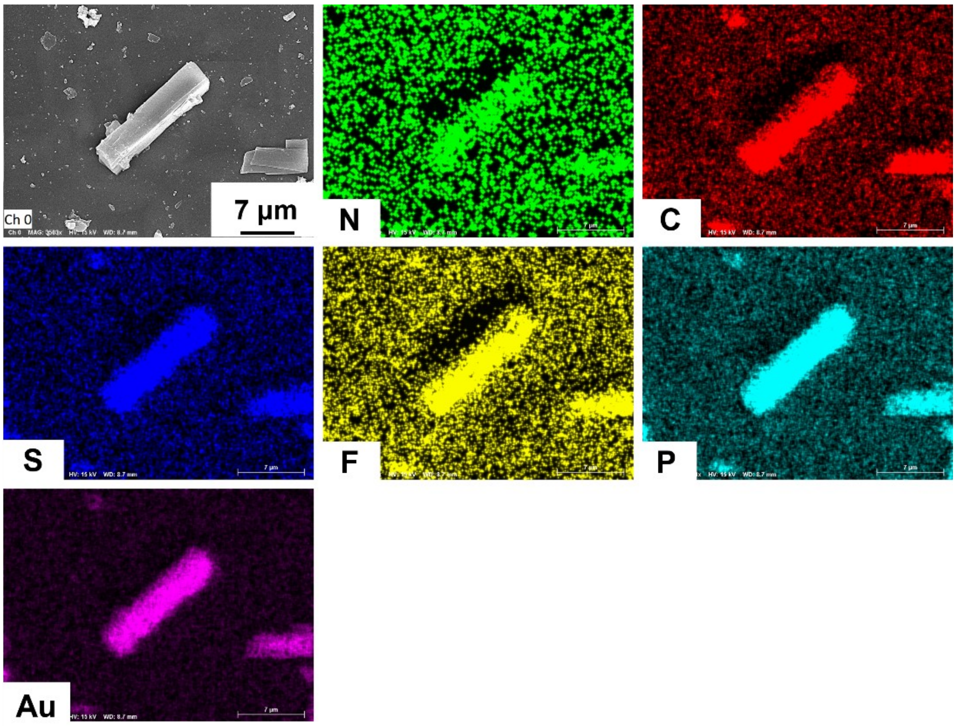

Figure S15. SEM patterns and elemental mapping images of cluster-based capsule [**C1**]$_2$•6PF$_6^-$ crystalline sample.

S3. X-ray Crystallography of Dimeric Capsule [C1]$_2$•6PF$_6^-$

X-ray diffraction data of the crystals of the dimeric capsule [**C1**]$_2$•6PF$_6^-$ were collected using a Bruker D8 Venture diffractometer. The diffraction data reduction and integration were performed by the Bruker SAINT software. Positions of the Au atoms and most of the non-hydrogen atoms were found using the direct methods program in the Bruker SHELXTL software package. SHELXT is the software by Sheldrick for the structure solution that typically uses Intrinsic Phase methods.[1] SHELXL is the software by Sheldrick for the structure refinement.[2] However, all hydrogen atoms were placed in calculated positions in the final structure refinement. Crystal structure refinement data are given in Table S1. The selected geometric parameters are shown in Tables S2-S4. In the dimeric capsule [**C1**]$_2$•6PF$_6^-$, the unit cell includes a large region of disordered solvent molecules and counter-anions, which could not be modeled as discrete atomic sites. We employed PLATON/SQUEEZE to calculate the diffraction contribution of the solvent molecules and anions. These data (CCDC 2301196) can be achieved via the Cambridge Crystallographic Data Centre deposit@ccdc.cam.Ac.uk, http://www.ccdc.cam.ac.uk/deposit.

Table S1. Crystallographic data of the dimeric capsule [**C1**]$_2$•6PF$_6^-$.

	[**C1**]$_2$•6PF$_6^-$
formula	C210 H222 Au12 F18 N12 P15 S12
FW	6468.85
crystal size [mm]	0.17 x 0.24 x 0.25
crystal system	trigonal
space group	R -3 c
a [Å]	34.3007 (7)
b [Å]	34.3007 (7)
c [Å]	37.7858 (7)
α [º]	90
β [º]	90
γ [º]	120
V [Å^3]	38500.4 (17)
Z	6
ρ_{calcd}, [g/cm^{-3}]	1.674

μ [mm^{-1}]	7.079
F(000)	18558.0
$2\theta_{max}$ [º]	29.536
no. unique data	5185
parameters	1879
GOF [F^2]^a	1.04
R [F^2>2σ(F^2)], wR[F^2]^b	0.0881, 0.2612

[a] GOF = $[w(F_o^2- F_c^2)^2]/(n - p)^{1/2}$, where n and p denote the number of data points and the number of parameters, respectively. [b] R1 = $(||F_o| - |F_c||)/|F_o|$; wR2 =$[w(F_o^2 - F_c^2)^2]/[w(F_o^2)^2]^{1/2}$,Where $w=1/[\sigma^2(F_o^2)+(aP)^2+bP]$ and $P=[\max(0, F_o^2)+2F_c^2]/3$.

Table S2. Selective bond distance (Å) and angle (°) of the dimeric capsule [**C1**]$_2$•6PF$_6^-$.

Bond	Dist.[Å]	Bond	Dist.[Å]
Au1-Au2	2.836(1)	C10-N1	1.31(2)
Au1-P1	2.256(4)	C10-S3	1.78(2)
Au1-S4	2.287(5)	C10-S4	1.69(2)
Au2-P3	2.265(4)	Au1-P1	2.256(6)
Au2-S3	2.322(4)	Au2-P3	2.265(6)
Au2-Au2	3.0279(9)	Au2-Au2	3.0279(9)
S3-Au2	2.322(5)	C11-P3	1.81(2)
S4-Au1	2.287(6)	C17-P1	1.80(2)
C5-N2	1.50(2)	C7-N1	1.45(3)
C6-N2	1.43(3)		

Bond	Angle [°]	Bond	Angle [°]
Au2-Au1-P1	92.9(1)	Au2-Au2-Au1	108.52(3)
Au2-Au1-S4	94.0(1)	Au2-Au2-P3	100.9(1)
P1-Au1-S4	172.7(2)	S3-Au2-Au1	91.6(1)
Au1-Au2-P3	92.3(1)	S3-Au2-P3	173.5(2)
Au1-Au2-S3	91.6(1)	Au1-Au2-P3	92.3(1)
Au1-Au2-Au2	108.53(3)	F7-P4-F8	168(2)
P3-Au2-S3	173.5(2)	F7-P4-P4	165(2)
P3-Au2-Au2	100.9(1)	F7-P4-F5	139(2)
S3-Au2-Au2	82.7(1)	F7-P4-F6	102(3)
C7-N1-C8	108(2)	F7-P4-F8	134(2)
C7-N1-C10	123(2)	F7-P4-P4	119(2)
C8-N1-C10	126(2)	F7-P4-F8	95(5)
C5-N2-C6	111(1)	F8-P4-P4	24(2)
C5-N2-C9	111(1)	F8-P4-F5	30(2)
Au1-P1-C17	114.1(6)	F8-P4-F6	82(3)
Au1-P1-C23	111.4(6)	F8-P4-F8	55(2)
Au1-P1-C24	110.9(5)	F1-F6-P4	105(4)
C17-P1-C23	107.1(8)	F1-F6-P4	113(5)
C17-P1-C24	106.5(7)	F1-F6-F1	5(4)
C23-P1-C24	106.4(8)	F1-F6-P4	120(5)
Au2-P3-C11	112.7(7)	P4-F6-P4	109(3)
Au2-P3-C23	112.3(6)	P4-F6-F1	100(5)
Au2-P3-C30	113.8(7)	P4-F6-P4	129(3)
C11-P3-C23	107.0(9)	P4-F6-F1	112(5)
C11-P3-C30	107.5(9)	P4-F6-P4	76(2)
C23-P3-C30	102.8(9)	F1-F6-P4	125(5)
S4-Au1-Au2	93.9(1)	P4-F8-F5	165(8)

S4-Au1-P1	172.8(2)	P4-F8-P4	61(4)
S4-Au1-Au2	94.0(2)	P4-F8-P4	89(5)
S4-Au1-P1	172.7(2)	F5-F8-P4	127(5)
Au2-Au1-P1	92.9(1)	F5-F8-P4	87(5)
Au2-Au2-S3	82.7(1)	P4-F8-P4	57(2)

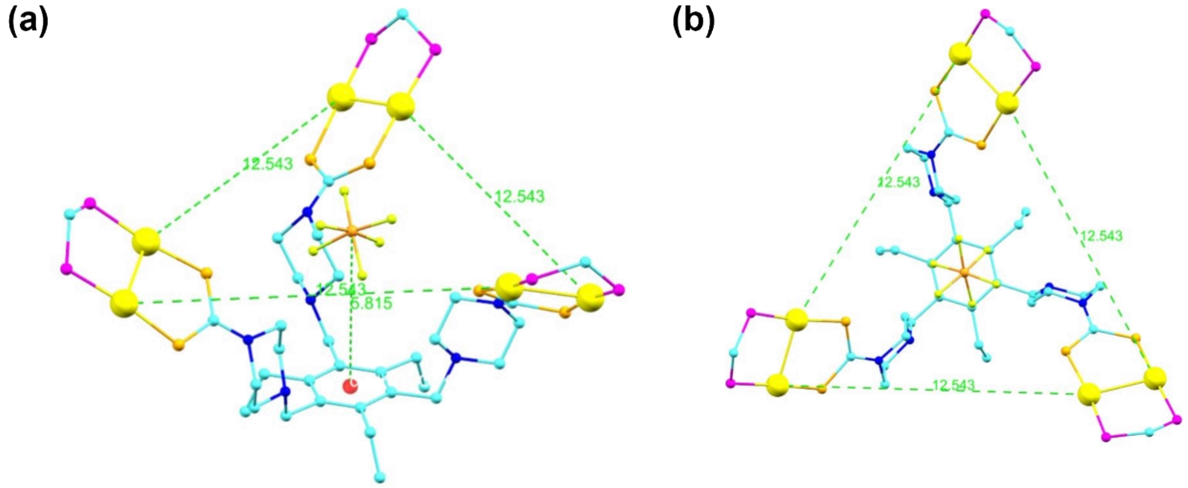

Figure S16. The half-bowl crystal structure of dimeric capsule [**C1**]$_2$•6PF$_6^-$ viewing along the *a*-axis (a) and *c*-axis (b).

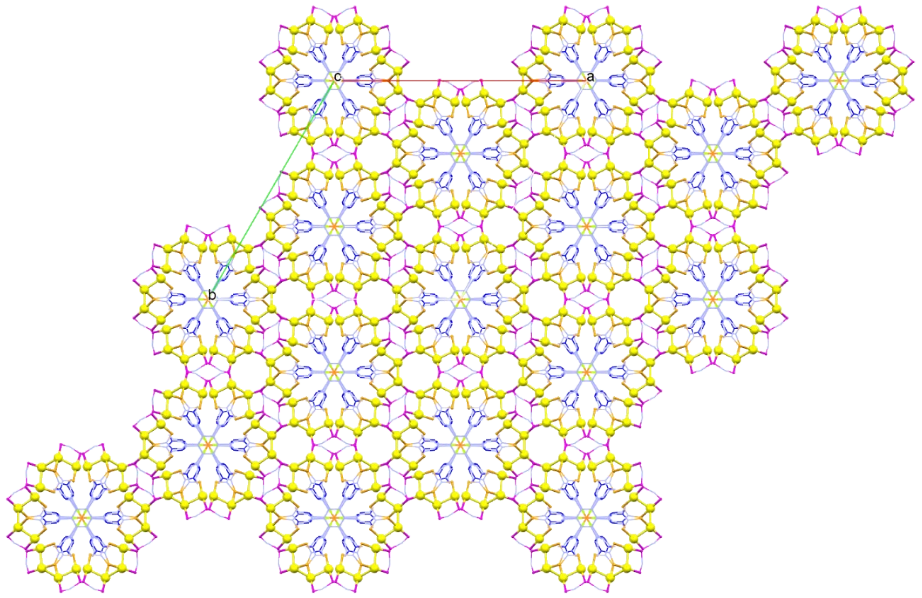

Figure S17. Packing of a 3-D molecular arrays in the crystal structure of dimeric capsule [**C1**]$_2$•6PF$_6^-$ viewing along the *c*-axis.

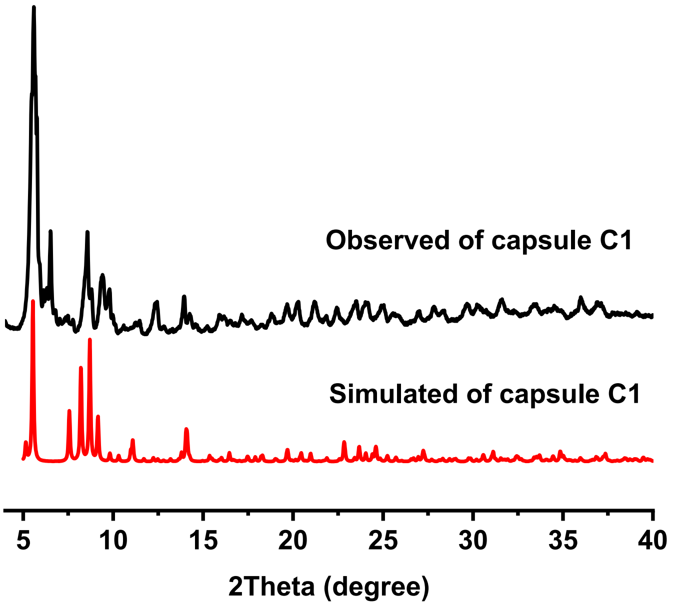

Figure S18. The PXRD profiles of dimeric capsule $[\mathbf{C1}]_2\bullet6PF_6^-$.

S4. Photophysical Data of Dimeric Capsule $[\mathbf{C1}]_2\bullet6PF_6^-$

Table S3. The photophysical data of dimeric capsule $[\mathbf{C1}]_2\bullet6PF_6^-$.

Cluster	Medium (T/K)	Uv-vis Absorbance λ/nm(Ɛ/M^{-1}·cm^{-1})	Excitation λ/nm	Emission λ/nm(τ_0/μs)	Φ
Capsule C1	CH_3CN (298)	267(9870) 355(1000)	374	487(6.57)	0.0330
	Solid (298)	279 389	467	546(5.42)	0.0177

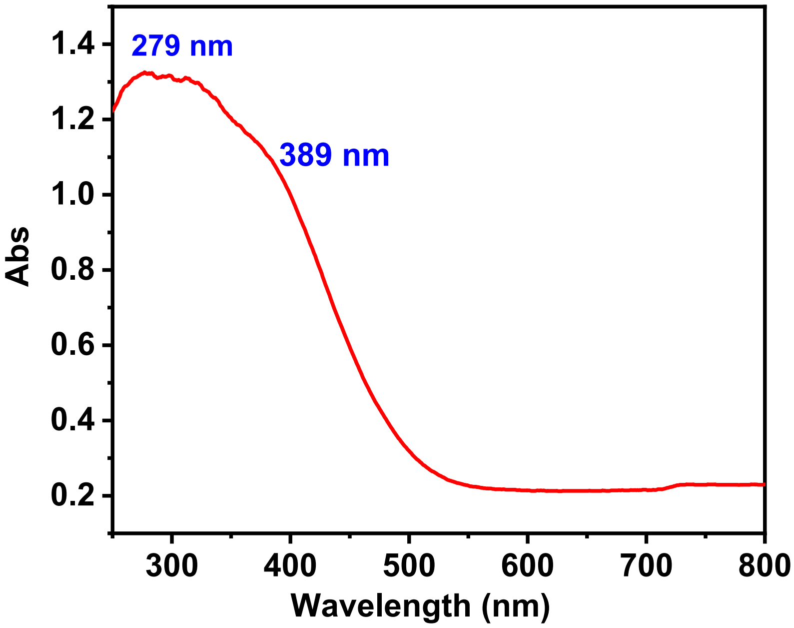

Figure S19. UV−vis diffuse reflectance spectra of dimeric capsule $[\mathbf{C1}]_2 \bullet 6PF_6^-$ in the solid state at 298 K.

Determination of dimerization constants by concentration-dependent UV-vis absorption studies [3-9]. The absorption bands that appear as the concentration of the complex increases are best interpreted in terms of an oligomerization of the gold(I) complex $[\mathbf{C1}]^{3+}$ cations. The equations (1) and (2) are the monomer-dimer equilibria respectively, where M = $[\mathbf{C1}]^{3+}$ and D = $[\mathbf{C1}_2]^{6+}$. In the analysis of these equilibria, (1) has been utilized to give the mathematical expressions of (2):

$$2\,\mathbf{M} \xrightleftharpoons{K_1} \mathbf{D} \qquad \mathbf{(1)}$$

$$\frac{[\mathrm{C}]}{\mathbf{A_2}^{1/2}} = \frac{\mathbf{1}}{(\boldsymbol{\varepsilon_2}\mathbf{K_1})^{1/2}} + \frac{\mathbf{2A_2}^{1/2}}{\boldsymbol{\varepsilon_2}} + \frac{\mathbf{3K_2A_2}}{\boldsymbol{\varepsilon_2}(\boldsymbol{\varepsilon_2}\mathbf{K_1})^{1/2}} \qquad \mathbf{(2)}$$

where [C] is the total concentration of the gold(I) complex, $\mathbf{A_2}$ is the absorbances due only to dimers, and $\boldsymbol{\varepsilon_2}$ is the corresponding molar extinction coefficients. By plotting $[\mathbf{C}]/\mathbf{A_2}^{1/2}$ against the dimer absorbance $\mathbf{A_2}$ as a straight line in equation (2), from the slope $(2/\boldsymbol{\varepsilon_2})$ and intercept $(1/(\boldsymbol{\varepsilon_2}\mathbf{K_1})^{1/2}$, the corresponding dimerization constant $\mathbf{K_1}$ can be determined.

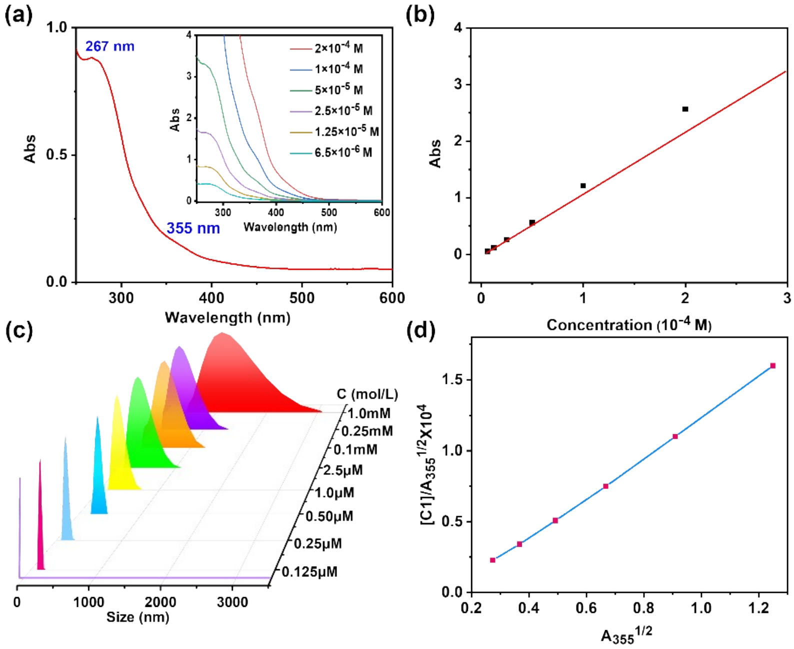

Figure S20. (a) UV-vis absorption spectrum of dimeric capsule [**C1**]$_2$•6PF$_6^-$ in CH$_3$CN as the concentration increases from 6.5 × 10^{-6} to 2.0 × 10^{-4} M at 298 K. (b) A plot of absorbance at 355 nm as a function of concentration for capsule [**C1**]$_2$•6PF$_6^-$. Experimental (■) and theoretical (red line) fit Beer's law. (c) Particle size distribution of the aggregated dimeric capsule [**C1**]$_2$•6PF$_6^-$ in solution (0.125 μM to 1.0 mM) determined by dynamic light scattering experiments. (d) Dimerization plot of monomer-dimer equilibrium in solution.

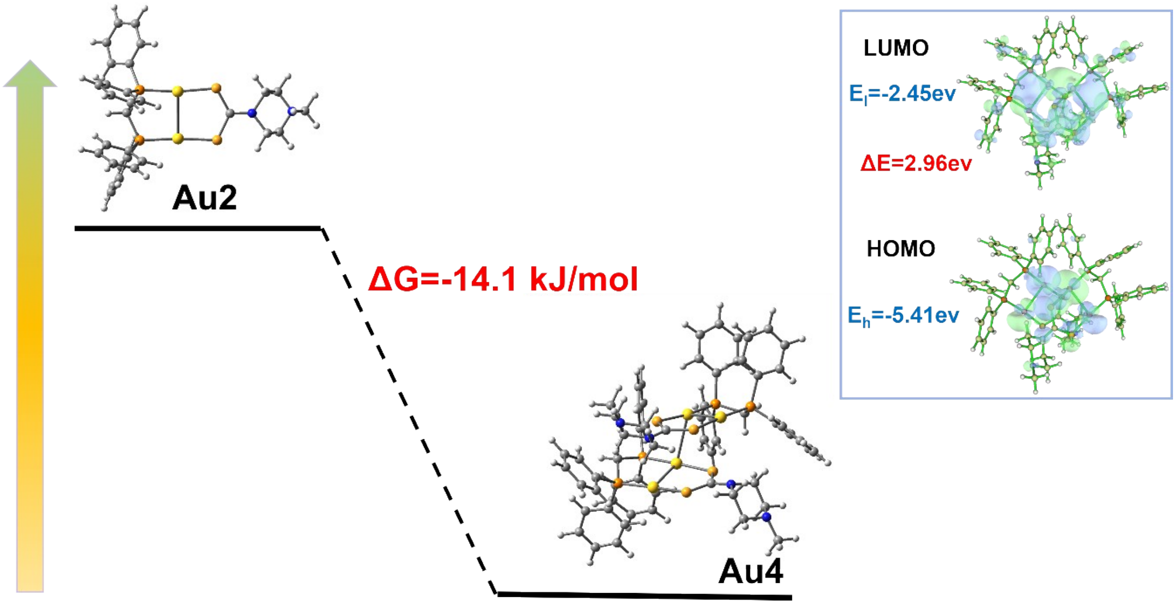

Figure S21. Schematic depiction of the optical band gap of spontaneous formation from Au2 to Au4.

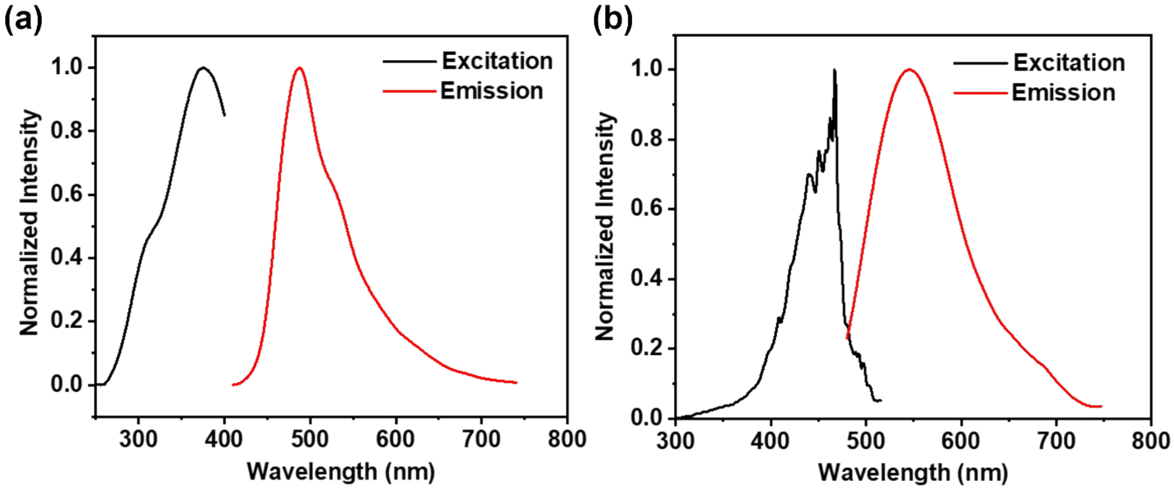

Figure S22. Excitation and emission spectra of dimeric capsule [**C1**]$_2$•6PF$_6^-$ (a) in CH_3CN solution (1×10^{-5} M) at 298 K; (b) in the solid state at 298 K.

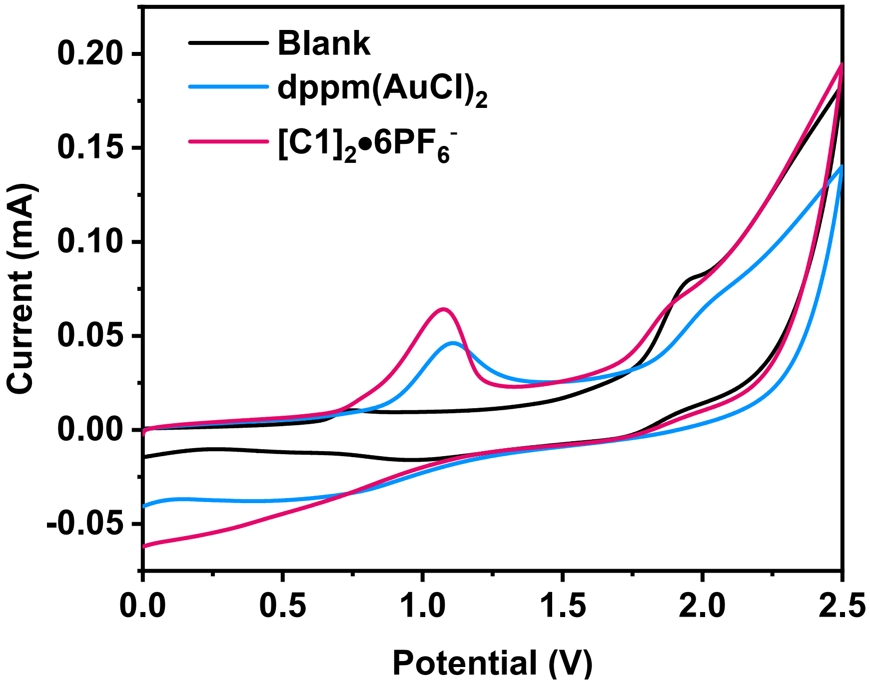

Figure S23. Cyclic voltammetry experiments (Ag/$AgNO_3$ was used as the reference electrode at a scan rate of 100 mV/s, Ep: peak potential). It was also concluded that the gold catalyst employed has one obvious oxidation peaks, the first being Au^{I}/Au^{II} (Ep = +1.07 V versus Ag/$AgNO_3$). [10]

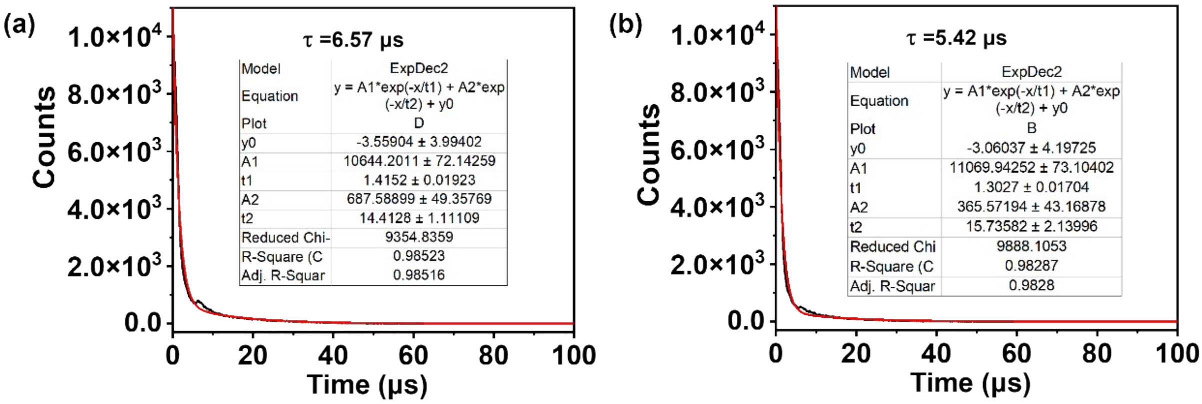

Model	ExpDec2
Equation	y = A1*exp(-x/t1) + A2*exp(-x/t2) + y0
Plot	D
y0	-3.55904 ± 3.99402
A1	10644.2011 ± 72.14259
t1	1.4152 ± 0.01923
A2	687.58899 ± 49.35769
t2	14.4128 ± 1.11109
Reduced Chi-	9354.8359
R-Square (C	0.98523
Adj. R-Squar	0.98516

Model	ExpDec2
Equation	y = A1*exp(-x/t1) + A2*exp(-x/t2) + y0
Plot	B
y0	-3.06037 ± 4.19725
A1	11069.94252 ± 73.10402
t1	1.3027 ± 0.01704
A2	365.57194 ± 43.16878
t2	15.73582 ± 2.13996
Reduced Chi	9888.1053
R-Square (C	0.98287
Adj. R-Squar	0.9828

Figure S24. Phosphorescence decay profiles and fitting curves of dimeric capsule [**C1**]$_2$•6PF$_6^-$: (a) in CH$_3$CN solution (1 × 10^{-5} M); (b) in the solid state at 298 K.

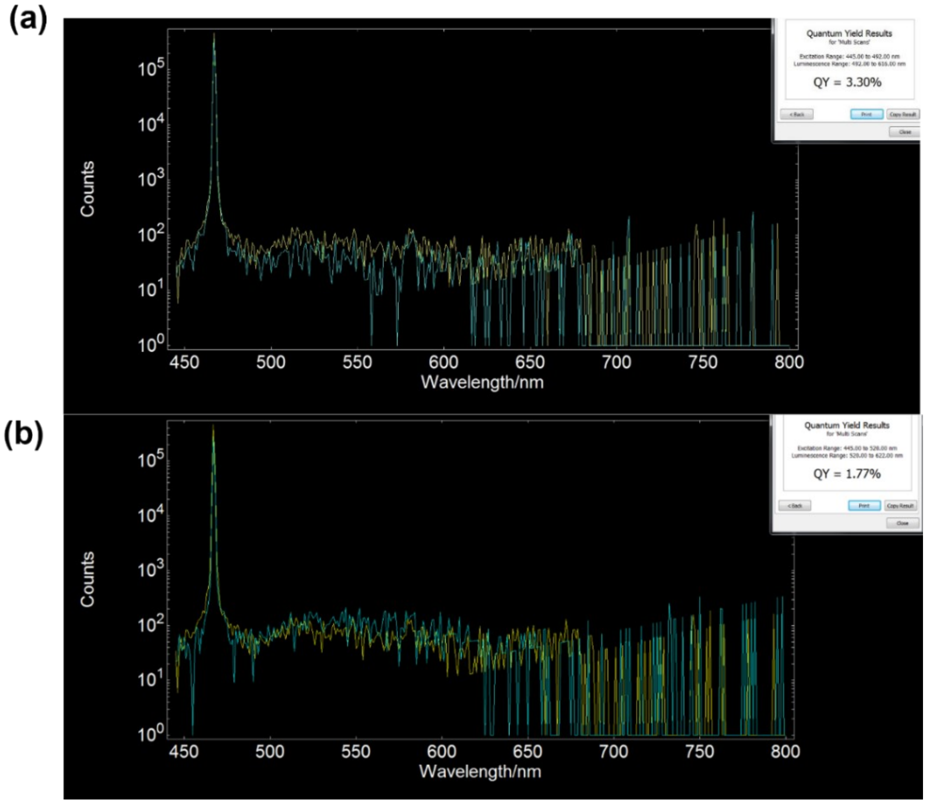

(a)
Quantum Yield Results
for 'Multi Scans'
Excitation Range: 445.00 to 492.00 nm
Luminescence Range: 492.00 to 616.00 nm
QY = 3.30%

(b)
Quantum Yield Results
for 'Multi Scans'
Excitation Range: 445.00 to 520.00 nm
Luminescence Range: 520.00 to 622.00 nm
QY = 1.77%

Figure S25. Quantum yield spectra of dimeric capsule [**C1**]$_2$•6PF$_6^-$: (a) in CH$_3$CN solution (1 × 10^{-5} M). (b) in the solid state at 298 K.

S5. General Protocol for Photocatalytic Oxidation

A glass tube was filled with a magnetic stir bar, the amine (0.5 mmol), crystalline samples of [**C1**]$_2$•6PF$_6^-$ (1.3 μmol, 8 mg) and CH$_3$CN (2 mL). The resulting mixture was stirred and irradiated with a 365 nm LED under air condition. After the catalytic reaction was stopped, the product was obtained by extracted with dichloromethane twice and filtrating for further determination.

Photoelectrochemical Measurements

$[\mathbf{C1}]_2\bullet 6PF_6^-$ (2 mg, 0.33 μmol) was dissolved in 1 mL of ethanol by ultrasound for 20 min to disperse completely. The working electrode was prepared by taking more than 20 μL of suspended liquid drops on the glass carbon electrode, with a Pt plate as the counter electrode, and an Ag/AgCl as a reference electrode to combine the standard three-electrode system. The electrolyte used was a 0.1 M deoxygenated Na_2SO_4 solution. A Mott-Schottky plot was recorded at frequencies of 500 Hz, 1000 Hz and 1500 Hz. Electrochemical impedance spectroscopy was acquired from 1 Hz to 100 kHz.

The photo-responsive signals were measured on a 365 nm LED as a light source and a standard three-electrode system. The working electrodes were prepared by coating the slurry on the surface of the FTO plate and covering approximately 1 cm^2. The Pt plate was used as the counter electrode, and an Ag/AgCl was a reference electrode. The electrolyte used was a 0.1 M deoxygenated Na_2SO_4 solution.

EPR Measurements

The EPR spectra were obtained in the presence of 5, 5-dimethyl-1-pyrroline-N-oxide (DMPO), 2, 2, 6, 6-Tetramethylpiperidoxyl (TEMPO) and 2, 2, 6, 6-Tetramethyl-4-piperidinone hydrochloride (TEMP) respectively. 10 μL DMPO was mixed with 190 μL of $[\mathbf{C1}]_2\bullet 6PF_6^-/CH_3CN$ suspension in the EPR tube under in situ illumination. Similarly, 10 μL TEMP or 10 μL TEMPO was mixed with 190 μL of $[\mathbf{C1}]_2\bullet 6PF_6^-/H_2O$ suspension in the EPR tube for in-situ illumination, respectively.

Table S4. Photo-oxidation of benzylamine to N-benzylbenzaldimine over different catalysts.

Entry	Catalyst	Light Source	t	Oxidant	T(°C)	Conversion (%)	Yield (%)	ΔE (eV)	Ref
1	**Capsule C1**	10W 365 nm LED	6h	air	RT	98	94	2.48	This work
2	HNU-64	300 W Xe lamp, >400 nm	7h	O_2 (1 atm)	25°C	93.2	90	2.52	11
3	Mn-PYTC$^+$	30W 405 nm LED	10h	air	RT	100	93	2.86	12
4	Au@ZrO_2 Pd@ZrO_2 Au-Pd@ZrO_2	500 W Hg lamp, 400-750nm	96h	O_2 (1 atm)	45°C	_	26 30 95	_	13
5	Zn-PDI	500 W Xe lamp, >420 nm	4h	air	RT	_	74	_	14
6	Zr-NDI-H_2DPBP	300 W Xe lamp	0.3h	O_2 (1 atm)	27°C	100	_	1.82	15
7	NaRh-SiW_{12}	10W white LED lamp	12h	O_2 (2 atm)	RT	_	96.1	2.25	16
8	Cd(dcbpy)	300 W Xe lamp	7h	air	25°C	99.1	98	3.48	17

Table S5. Optimization of Reaction Conditions.

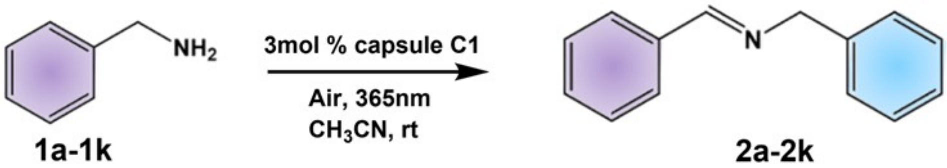

Entry	Catalyst	Deviation from standard condition	Conversion[b]	Yield[b]
1	Capsule **C1**	None	98%	94%
2	Capsule **C1**	N_2 atmosphere	trace	-
3	Capsule **C1**	dark	5%	3%
4	Capsule **C1**	O_2 atmosphere	98%	94%
5	None	Without photocatalyst	trace	-
6[c]	L^1	L^1 instead of Capsule **C1**	30%	12%
7[d]	dppmAu_2Cl_2	dppmAu_2Cl_2 instead of Capsule **C1**	trace	-
8	Capsule **C1**	heat instead of light	trace	-
9	Capsule **C1**	Acetone	trace	-
10	Capsule **C1**	CH_2Cl_2	89%	84%

[a] Standard conditions: 0.05 mmol benzylamine and 1.3 µmol [**C1**]$_2$•6PF_6^- in 2 mL CH_3CN irradiated with a 10 W 365 nm LED at room temperature in air for 6 h; [b] Conversion and yield of benzylamine coupling were detected using gas chromatography; [c] 5.0 µmol **L^1**; [d] 5.0 µmol dppmAu_2Cl_2.

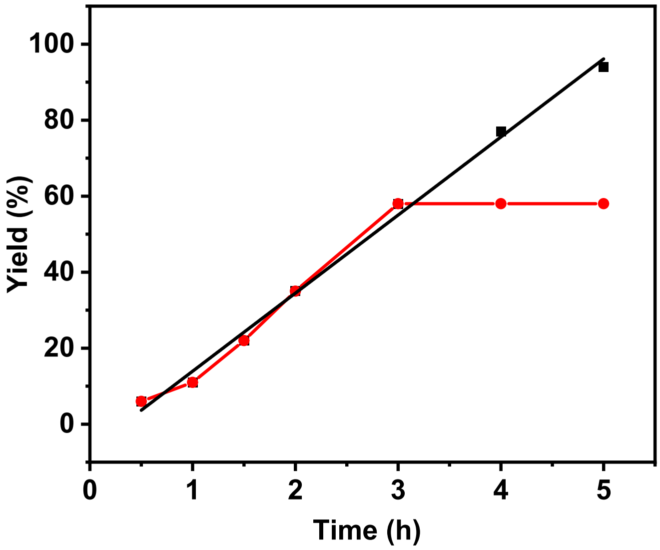

Figure S26. Time-dependent curves of the oxidative coupling of amines by capsule **C1** photocatalysis. (Dark: standard conditions. Red: the catalyst was filtered after 3 h).

Table S6. Scope of aerobic oxidative coupling of benzylamines.

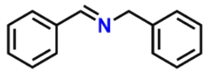

2a, 6h, 94%

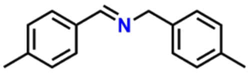

2b, 6h, 90%

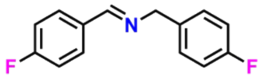

2c, 6h, 95%

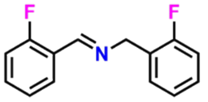

2d, 6h, 90%

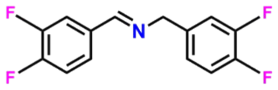

2e, 6h, 93%

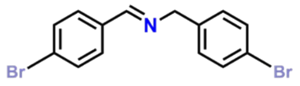

2f, 6h, 94%

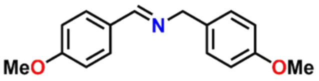

2g, 6h, 89%

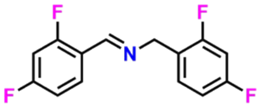

2h, 6h, 96%

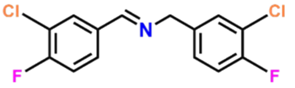

2i, 6h, 88%

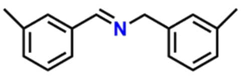

2j, 10h, 89%

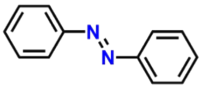

2k, 10h, 0%

[a] Standard conditions: benzylamine (0.05 mmol), capsule **C1** (3mol%) in CH_3CN (2 mL) irradiated with a 10 W 365 nm LED at room temperature under air for 6 h. [b] Yield benzylamine coupling are detected by gas chromatography.

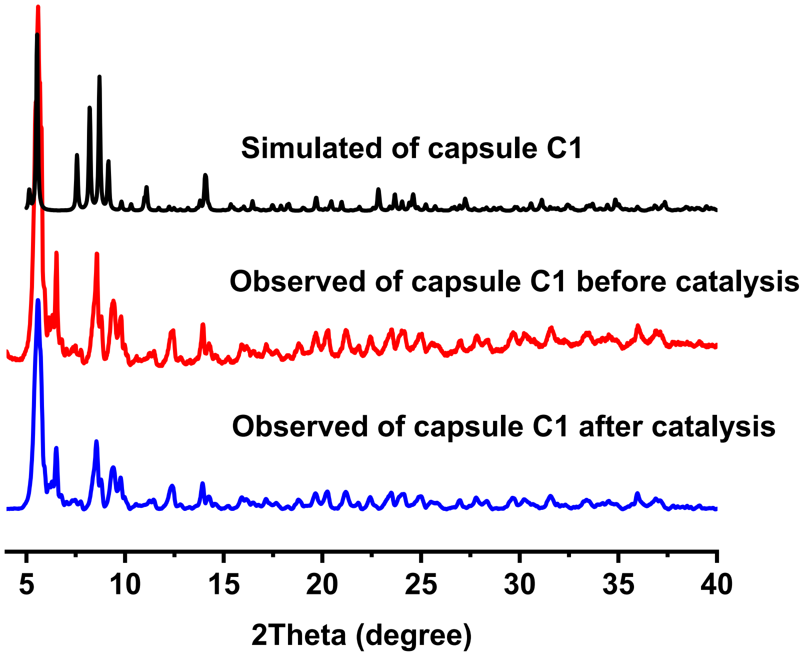

Figure S27. PXRD patterns of dimeric capsule $[\mathbf{C1}]_2 \bullet 6PF_6^-$ before and after catalysis.

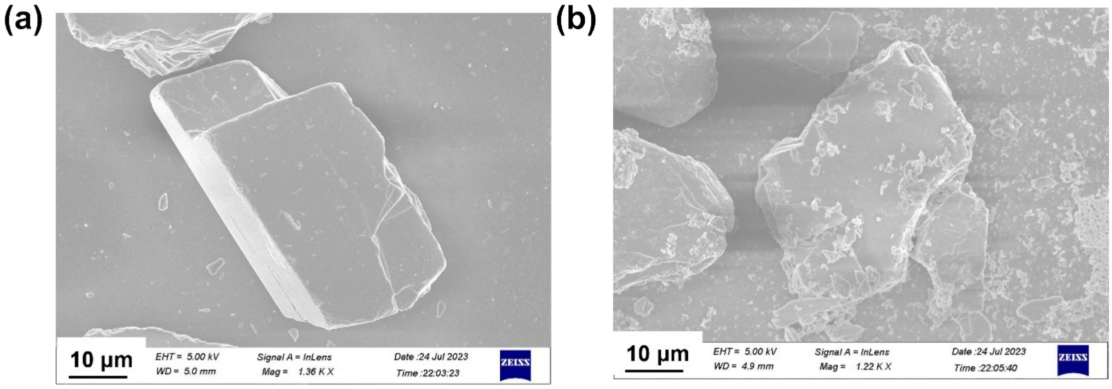

Figure S28. SEM patterns of dimeric capsule $[\mathbf{C1}]_2{\bullet}6PF_6^-$ before (a) and after catalysis (b).

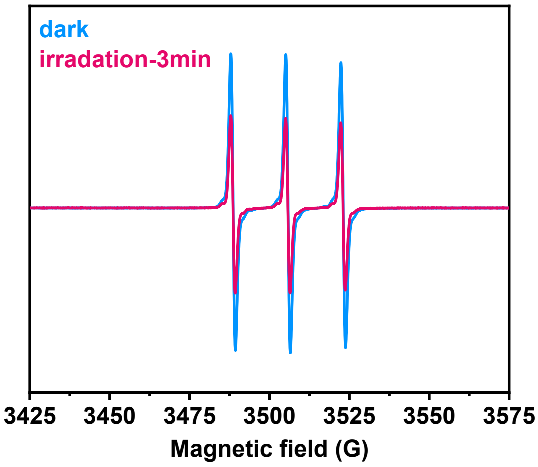

Figure S29. The EPR spectrum of photogenerated electron radicals trapped by TEMPO under continuous irradiation with a 365 nm LED light.

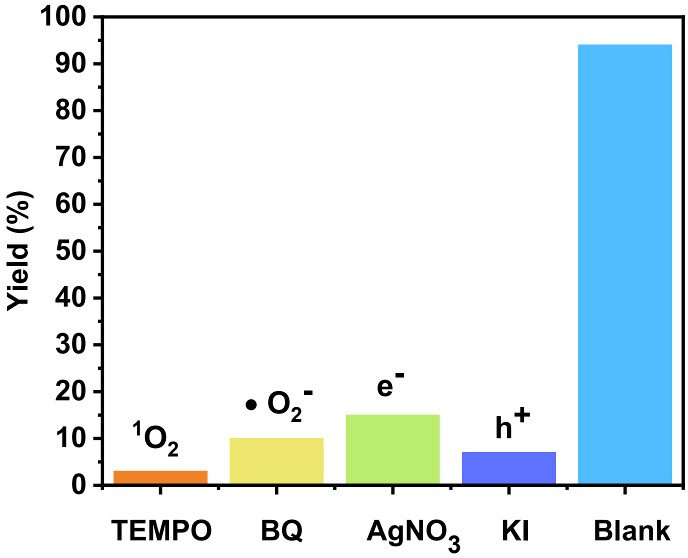

Figure S30. Quenching experiments to determine the active species.

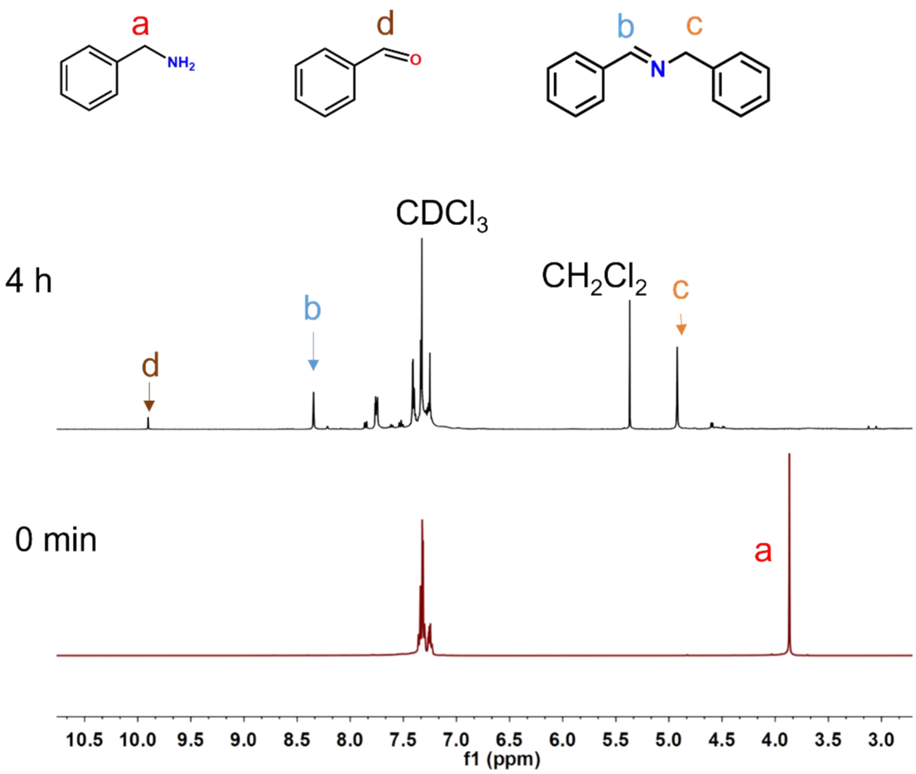

Figure S31. ^{1}H-NMR (298K, 400 MHz, $CDCl_3$-*d*) of dimeric capsule [**C1**]$_2$•6PF_6^- catalytic reaction system after 4 hours.

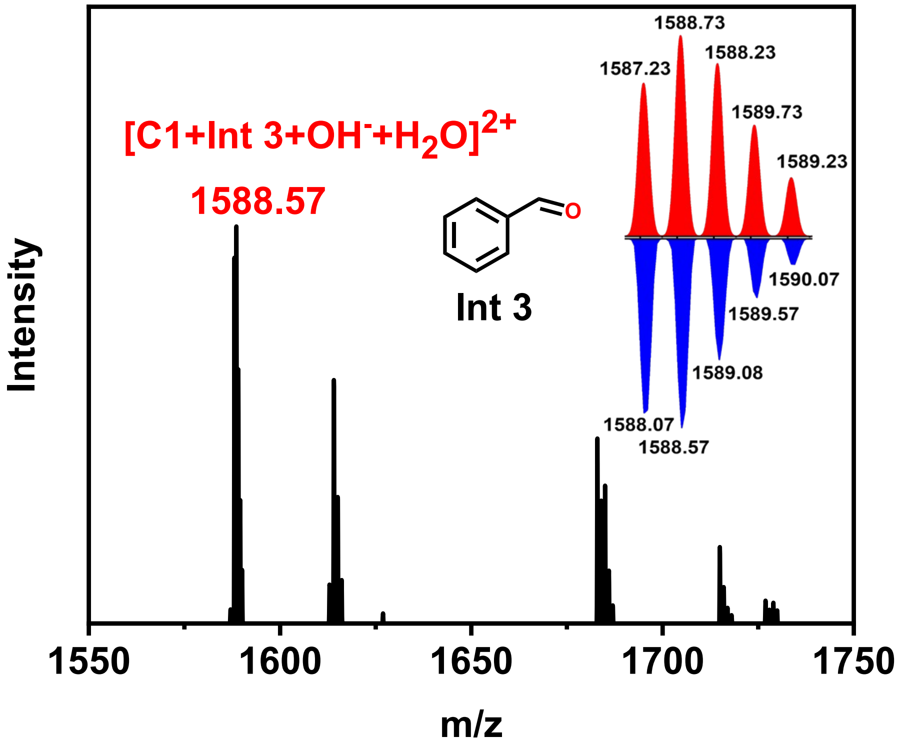

Figure S32. ESI-MS spectrum of the benzylamine oxidation mixture using dimeric capsule [**C1**]$_2$•6PF_6^- as a catalyst in CH_3CN at 298 K.

Detection of H_2O_2

The generation of H_2O_2 was determined indirectly by iodimetry methods through UV-vis spectroscopy. Adding 0.10 mL of the reaction supernatant to the mixture of 1.0 mL of 0.40 M KI and 1.0 mL of 0.10 M potassium hydrogen phthalate solutions, the liquid sample needed to be filled to 10 mL in a volumetric flask and kept over 20 minutes to make sure that I^- have completely formed to I_3^- by reacting with H_2O_2. Lastly, the mixture was measured by UV−vis spectroscopy. Black line (with benzylamine): The reaction of benzylamine with catalyst [**C1**]$_2$•6PF_6^- have produced H_2O_2, which made I^- completely convert to I_3^- as monitored by the UV absorption at 350 nm. Red line (no benzylamine): Without benzylamine, the solution of [**C1**]$_2$•6PF_6^- produced no H_2O_2. There was no signal at 350 nm in UV-Vis spectrum. Blue line (blank): Without benzylamine and catalyst, just KI and potassium hydrogen phthalate solutions.

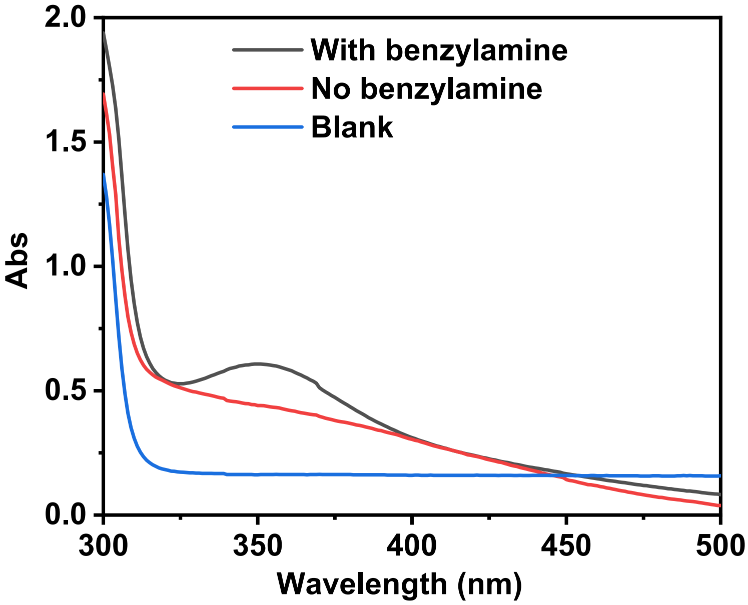

Figure S33. UV−vis absorption spectra of the indirectly iodimetry solution.

Detection of released NH_3

Benzylamine (0.050 mmol) and photocatalyst [**C1**]$_2$•6PF_6^- (8.0 mg) were stirred in CH_3CN (2.0 mL) under 365 nm LED irradiation for 6 h at room temperature in air. Then, 2.0 mL of distilled water was added to the solution, extracting 5.0 mL of CH_2Cl_2 three times. As shown in Figure S33, without catalyst [**C1**]$_2$•6PF_6^-, the pH value of the reaction solution did not change before and after, showing the pH at around 6-7. However, the pH of the fresh mixture of benzylamine and photocatalyst was 4-5 comparing with the test paper. Under 365 nm irradiation for 3 h, the aqueous layer was put to test its pH immediately, showing it pH = 7-8. After the reaction, the pH value could be 8-9, implying that the NH_3 molecule was released from the coupling reaction.

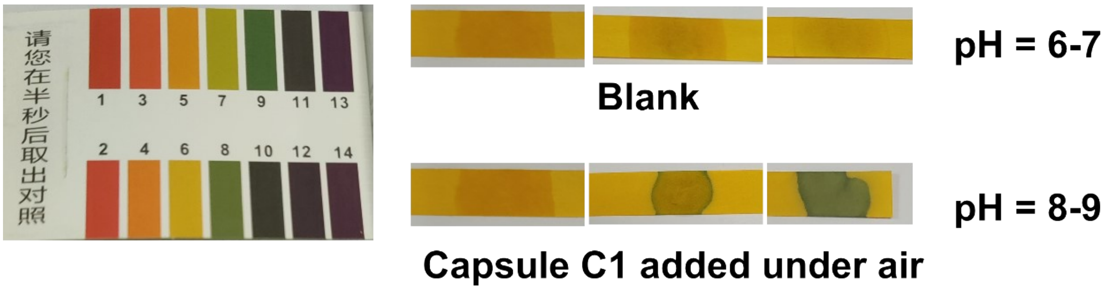

Figure S34. The pH test for the reaction solution after different conditions.

Characterization of the photocatalysis products

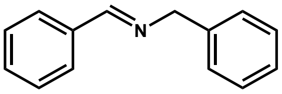

(E)-N-benzyl-1-phenylmethanimine (1a):

^{1}H NMR (298K, 400 MHz, CD_3CN-d_3) δ = 8.37 (s, 1H), 7.69-7.67 (m, 2H), 7.37-7.35 (m, 3H), 7.27-7.26 (d, J = 4.4 Hz, 4H), 7.20-7.15 (q, J = 4.3 Hz, 1H), 4.68 (s, 2H). GC-MS (CH_3CN, m/z): [**1a**]$^+$, calcd for 195, found, 195.1.

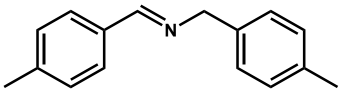

(E)-N-(4-methylbenzyl)-1-(p-tolyl)methanimine (1b):

^{1}H NMR (298K, 400 MHz, CD_3CN-d_3) δ = 8.31 (s, 1H), 7.57-7.55 (d, *J* = 8.0 Hz, 2H), 7.18-7.12 (dd, *J* = 14.8, 8.0 Hz, 4H), 7.08-7.06 (s, 2H), 4.61 (s, 2H), 2.28 (s, 3H), 2.22 (s, 3H). GC-MS (CH_3CN, m/z): [**1b**]$^+$, calcd for 223, found, 223.1.

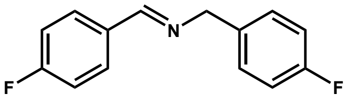

(E)-N-(4-fluorobenzyl)-1-(4-fluorophenyl)methanimine (1c):

^{1}H NMR (298K, 400 MHz, CD_3CN-d_3) δ = 8.46 (s, 1H), 7.85-7.82 (dd, *J* = 8.8, 5.6 Hz, 2H), 7.40-7.37 (dd, *J* = 8.7, 5.6 Hz, 2H), 7.23-7.18 (m, 2H), 7.13-7.09 (m, 2H), 4.76 (s, 2H). GC-MS (CH_3CN, m/z): [**1c**]$^+$, calcd for 231, found, 231.1.

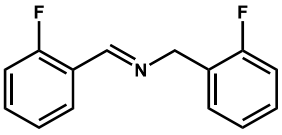

(E)-N-(2-fluorobenzyl)-1-(2-fluorophenyl)methanimine (1d):

^{1}H NMR (298K, 400 MHz, CD_3CN-*d_3*) δ 8.65 (s, 1H), 7.88-7.86 (m, 1H), 7.43 -7.36 (m, 1H), 7.33-7.32 (d, *J* = 5.9 Hz, 1H), 7.27-7.17 (m, 1H), 7.13-7.02 (m, 4H), 4.76 (s, 2H). GC-MS (CH_3CN, m/z): [**1d**]$^+$, calcd for 231, found, 231.1.

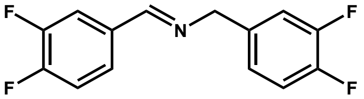

(E)-N-(3,4-difluorobenzyl)-1-(3,4-difluorophenyl)methanimine (1e):

^{1}H NMR (298K, 400 MHz, CD_3CN-*d_3*) δ = 8.31 (s, 1H), 7.48-7.47 (m, 2H), 7.27-7.09 (m, 2H), 4.65 (s, 2H). GC-MS (CH_3CN, m/z): [**1e**]$^+$, calcd for 267, found, 267.1.

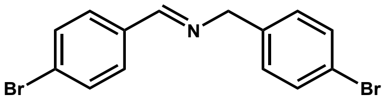

(E)-N-(4-bromobenzyl)-1-(4-bromophenyl)methanimine (1f):

^{1}H NMR (298K, 400 MHz, CD_3CN-*d_3*) δ = 8.33 (s, 1H), 7.70-7.68 (d, *J* = 9.6 Hz, 2H),7.59 (s, 1H), 7.53-7.51 (m, 2H), 7.43-7.40 (d, *J* = 8.5 Hz, 2H), 7.20-7.18 (d, *J* = 8.5 Hz, 2H), 4.64 (s, 2H). GC-MS (CH_3CN, m/z): [**1f**]$^+$, calcd for 353, found, 352.9.

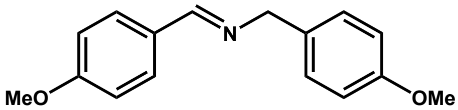

(E)-N-(4-methoxybenzyl)-1-(4-methoxyphenyl)methanimine (1g):

^{1}H NMR (298K, 400 MHz, CD_3CN-*d_3*) δ = 8.26 (s, 1H), 7.78-7.76 (d, *J* = 8.9 Hz, 2H), 7.62-7.60 (d, *J* = 8.8 Hz, 2H), 7.17-7.15 (d, *J* = 8.7 Hz, 1H), 7.00-6.98 (d, *J* = 8.8 Hz, 1H), 6.89-6.87 (d, *J* = 8.8 Hz, 1H), 6.82-6.79 (d, *J* = 8.8 Hz, 1H), 4.57 (s, 2H), 3.79 (s, 3H), 3.68 (s, 3H). GC-MS (CH_3CN, m/z): [**1g**]$^+$, calcd for 255, found, 255.1.

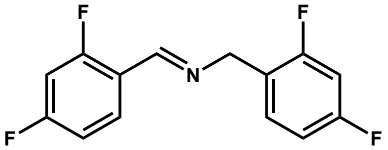

(E)-N-(2,4-difluorobenzyl)-1-(2,4-difluorophenyl)methanimine (1h):

^{1}H NMR (298K, 400 MHz, CD_3CN-*d_3*) δ = 8.58 (s, 1H), 6.96-6.93 (d, *J* = 8.7 Hz, 2H), 6.91-6.88 (t, *J* = 8.8 Hz, 4H), 4.71 (s, 2H). GC-MS (CH_3CN, m/z): [**1h**]$^+$, calcd for 267, found, 267.1.

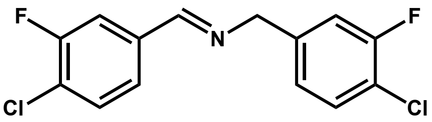

(E)-N-(4-chloro-3-fluorobenzyl)-1-(4-chloro-3-fluorophenyl)methanimine (1i):

^{1}H NMR (298K, 400 MHz, CD_3CN-*d₃*) δ = 8.33 (s, 1H), 7.61-7.59 (m, 1H), 7.48-7.47 (d, *J* = 4.1 Hz, 2H), 7.38-7.34 (d, *J* = 8.0 Hz, 1H), 7.20-7.17 (d, *J* = 10.5 Hz, 1H), 7.10-7.08 (d, *J* = 8.3 Hz, 1H), 4.68 (s, 2H). GC-MS (CH_3CN, m/z): [**1i**]$^+$, calcd for 299, found, 299.

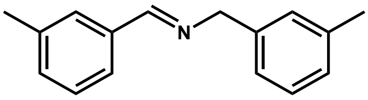

(E)-N-(3-methylbenzyl)-1-(p-tolyl)methanimine (1j):

^{1}H NMR (298K, 400 MHz, CD_3CN-*d₃*) δ = 8.43 (s, 1H), 7.74 -7.73 (m, 2H), 7.53-7.51 (d, *J* = 7.7 Hz, 2H), 7.35-7.33 (d, *J* = 7.6 Hz, 2H), 7.119-7.14 (d, *J* = 11.5 Hz, 2H), 4.75 (d, *J* = 1.3 Hz, 2H), 2.39 (s, 3H), 2.35 (s, 3H). GC-MS (CH_3CN, m/z): [**1j**]$^+$, calcd for 223, found, 223.1.

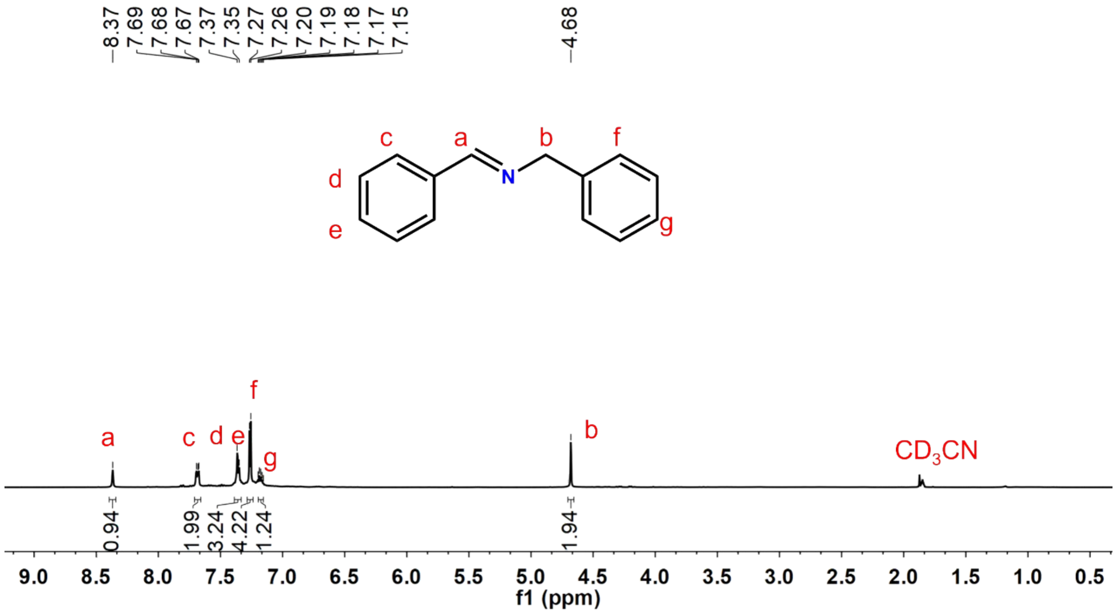

Figure S35. ^{1}H-NMR (298 K, 400 MHz, CD_3CN-*d₃*) of (E)-N-benzyl-1-phenylmethanimine (**1a**).

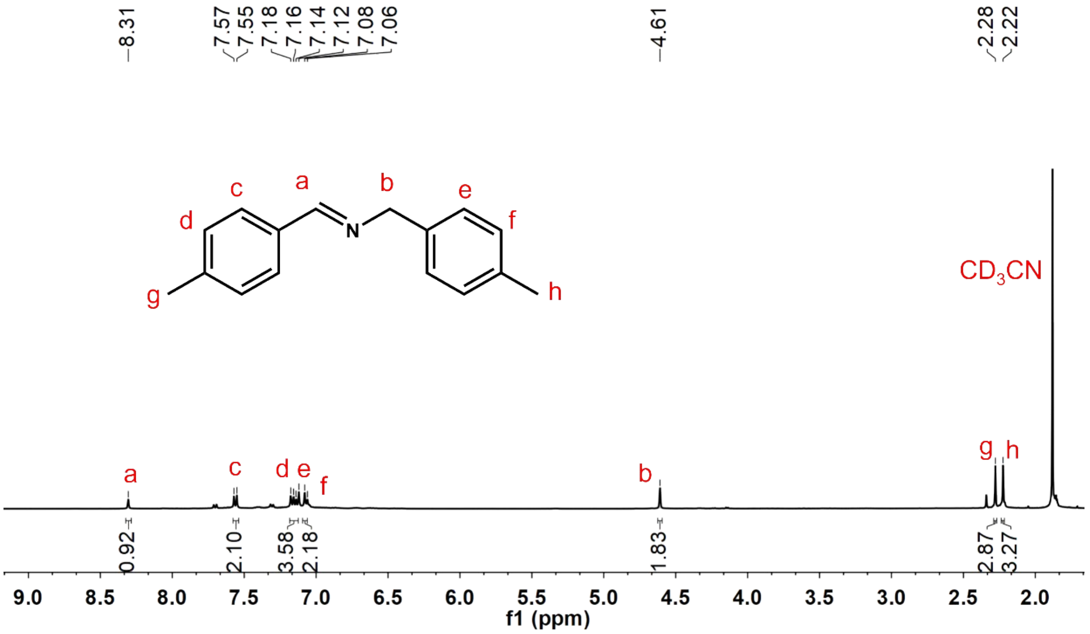

Figure S36. ^{1}H-NMR (298 K, 400 MHz, CD$_3$CN-*d$_3$*) of (E)-N-(4-methylbenzyl)-1-(p-tolyl)methanimine (**1b**).

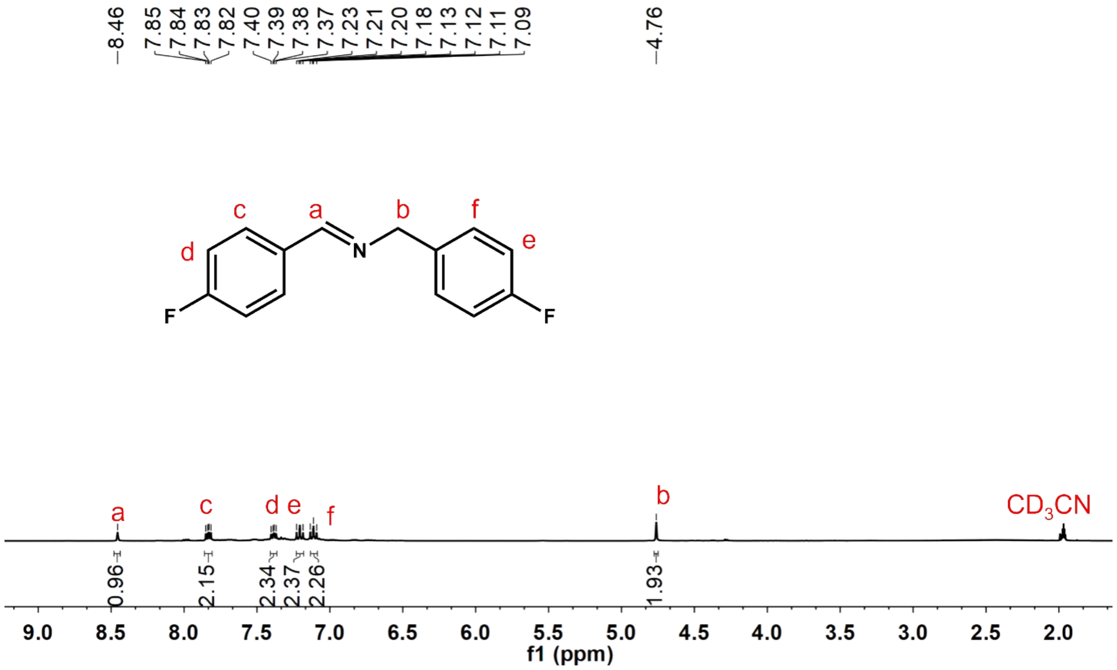

Figure S37. ^{1}H-NMR (298 K, 400 MHz, CD$_3$CN-*d$_3$*) of (E)-N-(4-fluorobenzyl)-1-(4-fluorophenyl)methanimine (**1c**).

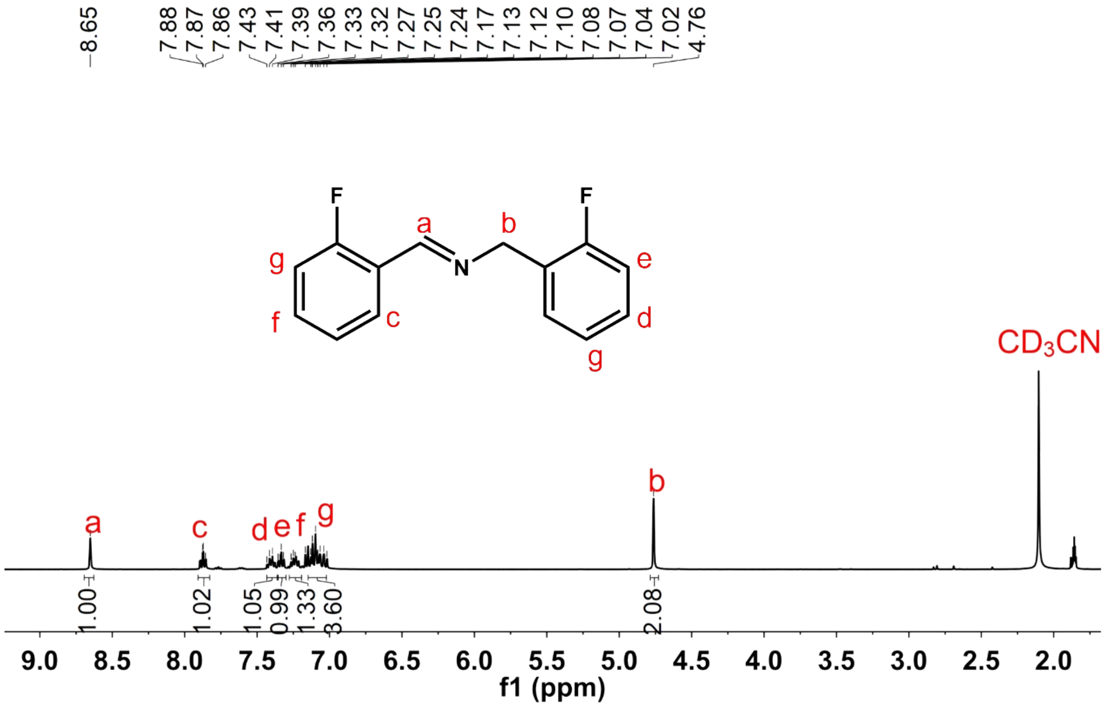

Figure S38. ^{1}H-NMR (298 K, 400 MHz, CD_3CN-*d₃*) of (E)-N-(2-fluorobenzyl)-1-(2-fluorophenyl)methanimine (**1d**).

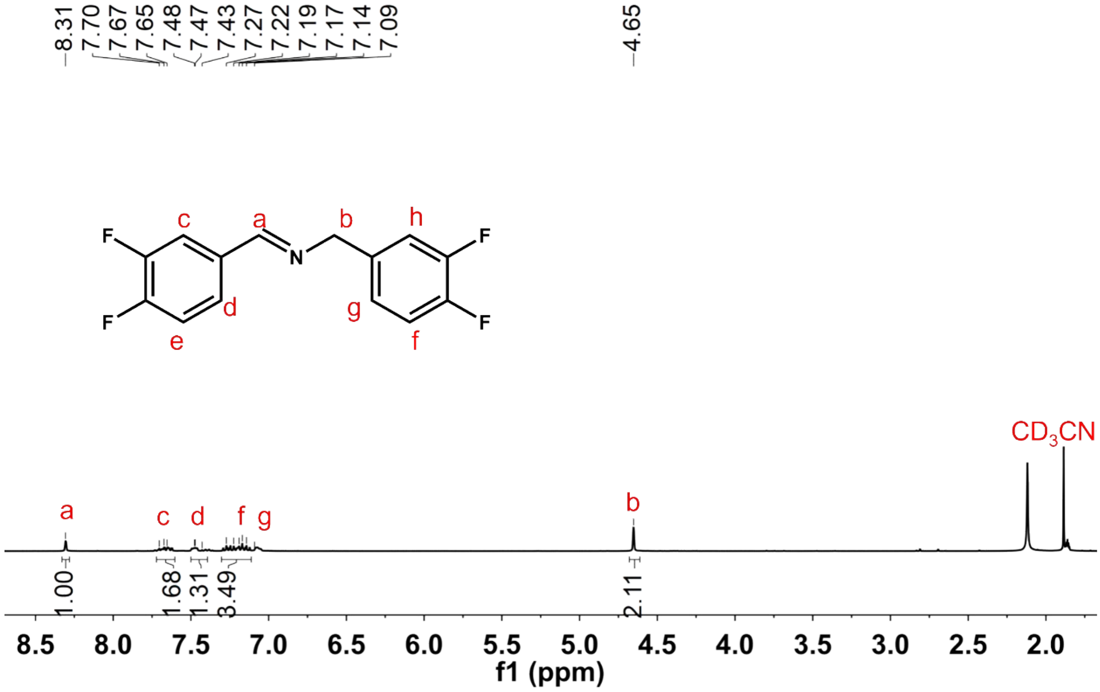

Figure S39. ^{1}H-NMR (298 K, 400 MHz, CD_3CN-d_3) of (E)-N-(3,4-difluorobenzyl)-1-(3,4-difluorophenyl)methanimine (**1e**).

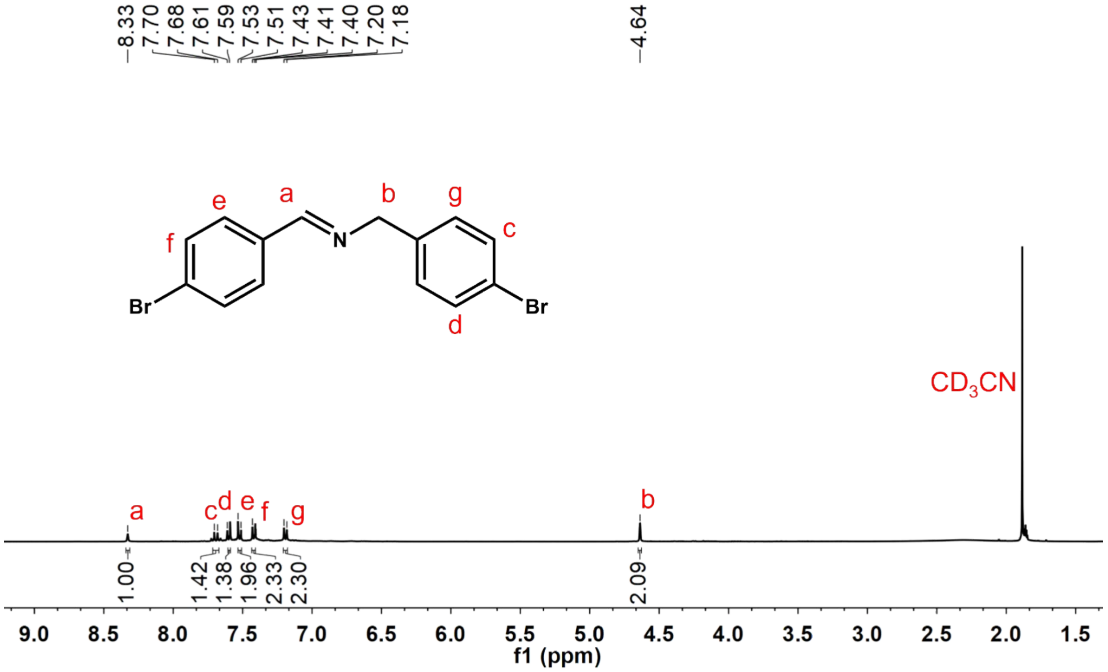

Figure S40. ^{1}H-NMR (298 K, 400 MHz, CD_3CN-*d₃*) of (E)-N-(4-bromobenzyl)-1-(4-bromophenyl)methanimine (**1f**).

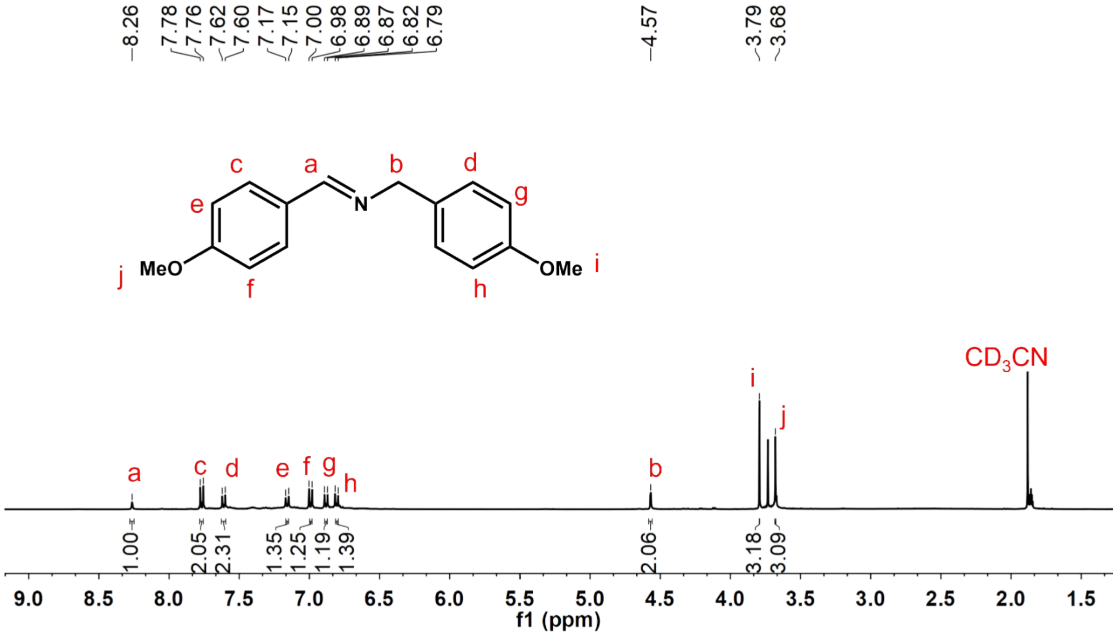

Figure S41. ^{1}H-NMR (298 K, 400 MHz, CD_3CN-d_3) of (E)-N-(4-methoxybenzyl)-1-(4-methoxyphenyl)methanimine (**1g**).

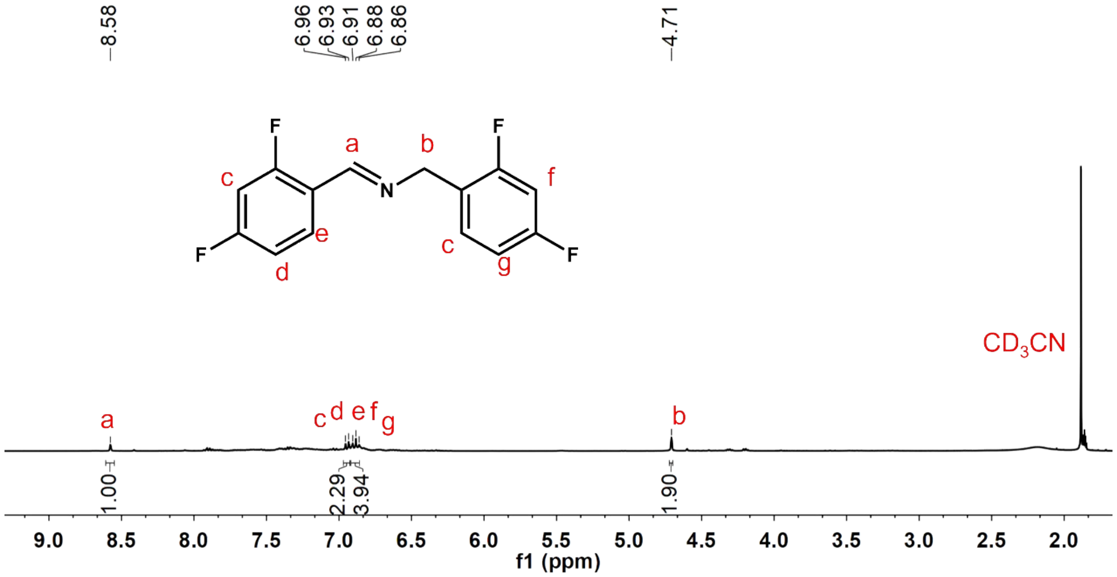

Figure S42. ^{1}H-NMR (298 K, 400 MHz, CD_3CN-*d₃*) of (E)-N-(2,4-difluorobenzyl)-1-(2,4-difluorophenyl)methanimine (**1h**).

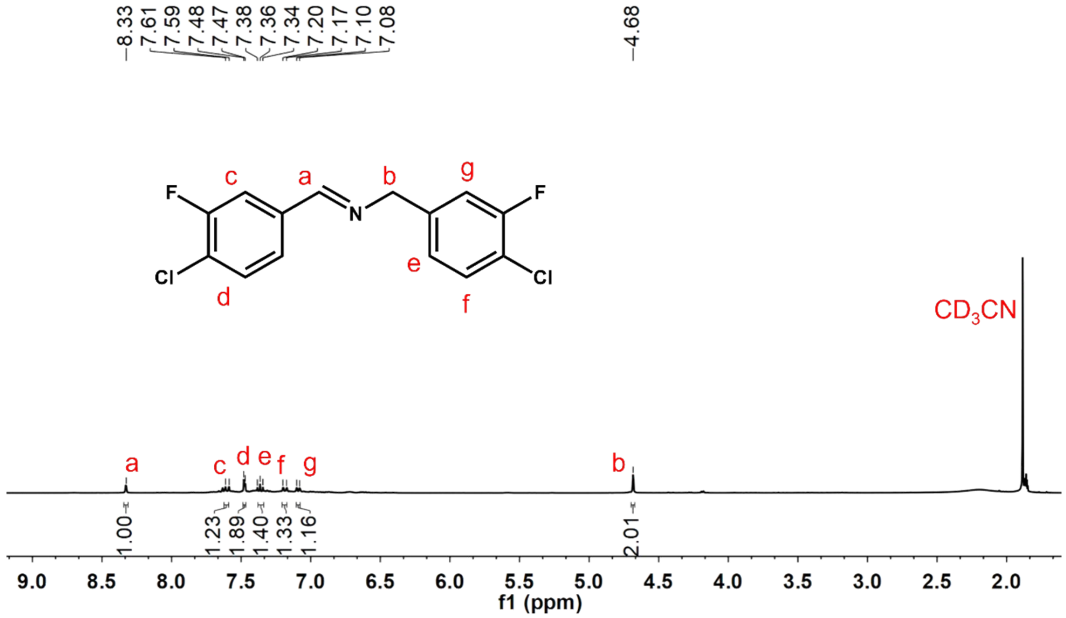

Figure S43. ^{1}H-NMR (298 K, 400 MHz, CD_3CN-d_3) of (E)-N-(4-chloro-3-fluorobenzyl)-1-(4-chloro-3-fluorophenyl)methanimine (**1i**).

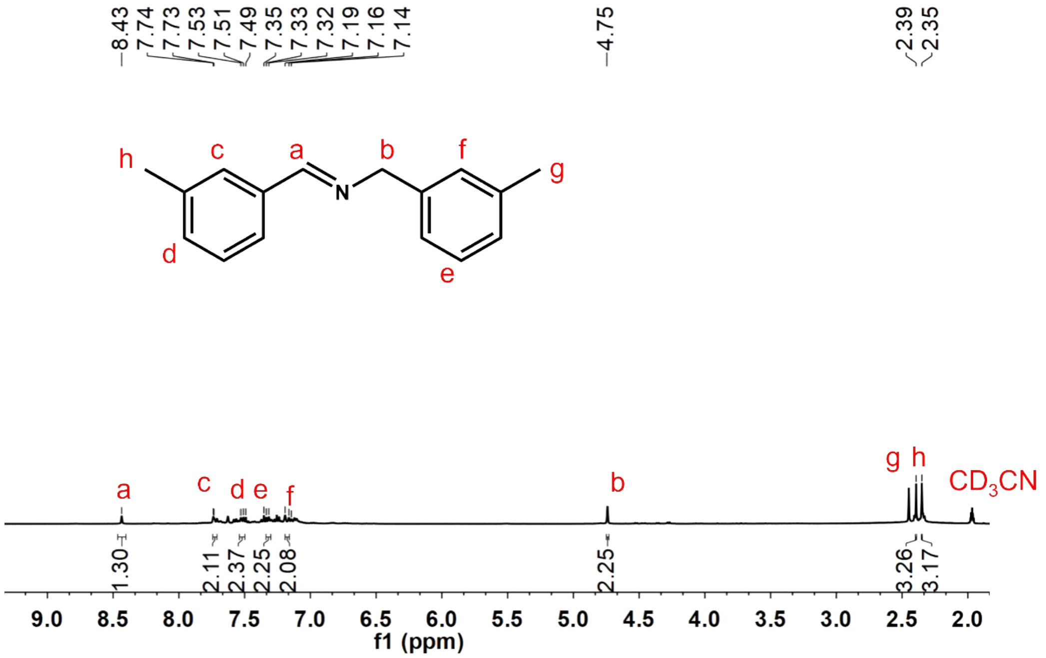

Figure S44. ^{1}H-NMR (298 K, 400 MHz, CD_3CN-*d*$_3$) of (E)-N-(3-methylbenzyl)-1-(p-tolyl)methanimine (**1j**).

S6. DFT Calculation for Photocatalytic Benzylamine Oxidation Mechanism

All geometries were fully optimized via density functional theory using the M06L [18-20] functional. Geometry optimizations were performed with the 6-31G (d) [21-22] basis set for main-group elements and the SDD [23-24] basis set for Au atom. In addition, restricted optimization is applied to all atoms except hydrogen atoms in the structure. All structures have been optimized considering solvent effects using the PCM [25-26] model for acetonitrile. Vibrational frequency analyses at the same level of theory were performed on all optimized structures to characterize stationary points as local minima or transition states. Furthermore, intrinsic reaction coordinate (IRC) computations were carried out to confirm that transition states connect to the appropriate reactants and products. The single-point energy calculations were carried out using the the 6-311++g (d, p) basis set [27] to provide better energy correction. The final E value is calculated from the high precision single point energy plus the zero-point energy correction. All DFT theoretical calculations have been carried out using the Gaussian 09 program [28-29].

Table S7. Some bonds distances (Å) in the molecular structures of the intermediates **TS 1, TS 1-2, TS2** and **TS2-2** in the pathway I and pathway II, respectively.

Pathway	Entry	Bond	Dist. [Å]	Entry	Bond	Dist. [Å]
Pathway I	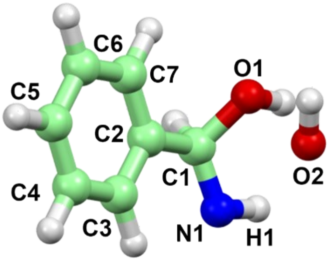 **TS 1**	C1-C2	1.514	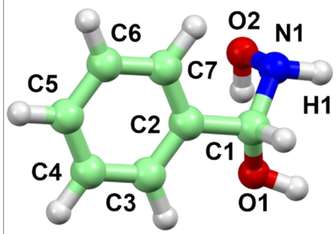 **TS 1-2**	C1-C2	1.517
		C1-N1	1.356		C1-N1	1.451
		C1-O1	1.448		C1-O1	1.419
		N1-O1	2.382		N1-O1	2.378
		N1-H1	1.022		N1-H1	1.022
		O1-O2	1.913		O1-O2	2.699
		O2-H1	2.813		C1-O2	2.312
Pathway II	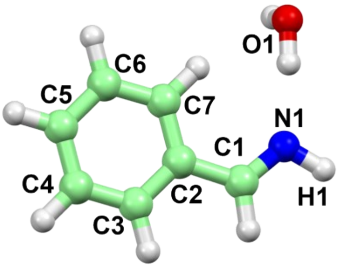 **TS 2**	C1-C2	1.475	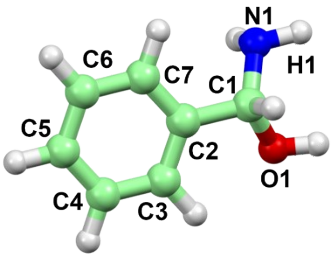 **TS 2-2**	C1-C2	1.520
		C1-N1	1.273		C1-N1	1.444
		C1-O1	3.837		C1-O1	1.421
		N1-O1	2.866		N1-O1	2.407
		N1-H1	1.020		N1-H1	1.017

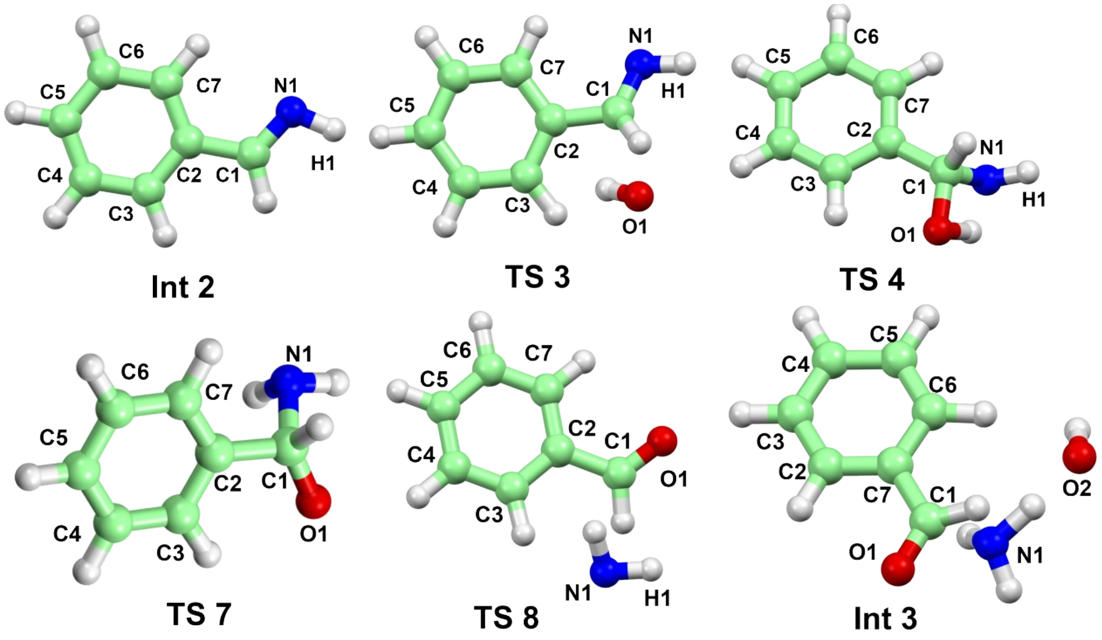

Int 2 **TS 3** **TS 4**

TS 7 **TS 8** **Int 3**

Figure S45. The molecular structures of intermediates **Int 2-Int 3** in the pathway III.

Table S8. Some bonds distances (Å) in the molecular structures of the intermediate **Int 2-Int 3** in the pathway III.

Entry	Bond	Dist. [Å]	Entry	Bond	Dist. [Å]
Int 2	C1-C7	1.479	**TS 3**	C1-C7	1.496
	C1-N1	1.272		C1-N1	1.289
	C1-O1	1.883		C1-O1	2.294
	N1-O1	2.411		N1-O1	3.071
	N1-H1	1.021		N1-H1	1.021
TS 4	C1-C7	1.526	**TS 6**	C1-C7	1.548
	C1-N1	1.468		C1-N1	1.533
	C1-O1	1.411		C1-O1	1.313
	N1-O1	2.209		N1-O1	2.392
	N1-H1	1.024		N1-H1	2.440
TS 8	C1-C7	1.490	**Int 3**	C1-C7	1.502
	C1-N1	2.956		C1-N1	2.251
	C1-O1	1.222		C1-O1	1.230
	N1-O1	3.773		N1-O1	2.947
	N1-H1	1.033		N1-H1	3.590

S7. References

[1] L. J. Barbour, X-Seed 4: Updates to A Program for Small-Molecule Supramolecular Crystallography. *J. Appl. Crystallogr.* **2020**, *53*, 1141-1146.

[2] G. M. Sheldrick, Crystal Structure Refinement with SHELXL. *Acta Crystallogr C.* **2015**, *71*, 3-8.

[3] K. R. Mann, N. S. Lewis, R. M. Williams, H. B. Gray, J. G. Gordon, Further Studies of Metal-Metal Bonded Oligomers of Rhodium(I) Isocyanide Complexes. Crystal Structure Analysis of Octakis(phenyl isocyanide)dirhodium Bis(tetraphenylborate). *Inorg. Chem.* **1978**, *17*, 828-834.

[4] C. Po, A. Y.-Y. Tam, K. M.-C. Wong, V. W.-W. Yam, Supramolecular Self-Assembly of Amphiphilic Anionic Platinum(II) Complexes: A Correlation between Spectroscopic and

Morphological Properties. *J. Am. Chem. Soc.* **2011**, *133*, 12136-12143.

[5] A. K. W. Chan, K. M.-C. Wong, V. W.-W. Yam, Supramolecular Assembly of Isocyanorhodium(I) Complexes: an Interplay of Rhodium(I)···Rhodium(I) Interactions, Hydrophobic-hydrophobic Interactions, and Host−Guest Chemistry. *J. Am. Chem. Soc.* **2015**, *137*, 6920-6931.

[6] K. M.-Ch. Wong, N.-Y. Zhu, V. W.-W. Yam, Unprecedent Formation of an Acetamidate-Bridged Dinuclear Platinum(II) Terpyridyl Complex-correlation of Luminescence Properties with the Crystal Forms and Dimerization Studies in Solution. *Chem. Commun.* **2006**, 3441-3443.

[7] S.-Y. Yu, Z.-X. Zhang, E. C.-C. Cheng, Y.-Z. Li, V. W.-W. Yam, H.-P. Huang, R. Zhang, A Chiral Luminescent Au16 Ring Self-Assembled from Achiral Components. *J. Am. Chem. Soc.***2005**， *127*， 17994-17995.

[8] S. -Y. Yu, Q. -F. Sun, T. K. -M. Lee, E. C. -C. Cheng, Y. -Z. Li, V. W.-W. Yam, Au36 Crown: A Macrocyclization Directed by Metal–Metal Bonding Interactions. *Angew. Chem. Int. Ed.* **2008**, *47*, 4551-4554.

[9] Q. -F. Sun, T. K. -M. Lee, P. -Z. Li, L. -Y. Yao, J. -J. Huang, J. Huang, S. -Y. Yu, Y. -Z. Li, V. W.-W. Yam, Self-assembly of a Neutral Luminescent Au12 Cluster with D2 Symmetry. *Chem. Commun*. **2008**, *43*, 5514-5516.

[10] H. Liang, Y. Julaiti, C.-G. Zhao, J. Xie, Electrochemical Gold-Catalysed Biocompatible C (sp^2)-C (sp) Coupling. *Nat. Synth.* **2023**, *2*, 338-347.

[11] G. Che, W.-T. Yang, C. Wang, M.-L. Li, X.-Y. Li, Q.-H. Pan, Efficient Photocatalytic Oxidative Coupling of Benzylamine over Uranyl-Organic Frameworks. *Inorg. Chem.* **2022**, *61*, 12301-12307.

[12] Q. Zhang, Y. Jin, L. Ma, Y. Zhang, C. Meng, C. Duan, Chromophore-Inspired Design of Pyridinium-Based Metal-Organic Polymers for Dual Photoredox Catalysis. *Angew. Chem. Int. Edit.* **2022**, *61*, e202204918.

[13] S. Sarina, H. Zhu, E. Jaatinen, Q. Xiao, H. Liu, J. Jia, C. Chen and J. Zhao, Enhancing Catalytic Performance of Palladium in Gold and Palladium Alloy Nanoparticles for Organic Synthesis Reactions through Visible Light Irradiation at Ambient Temperatures. *J. Am. Chem. Soc.* **2013**, *135*, 5793-5801.

[14] L. Zeng, T. Liu, C. He, D. Shi, F. Zhang and C. Duan, Organized Aggregation Makes Insoluble Perylene Diimide Efficient for the Reduction of Aryl Halides via Consecutive Visible Light-Induced Electron-Transfer Processes. *J. Am. Chem. Soc.* **2016**, *138*, 3958-3961.

[15] W.-J. Xu, B.-X. Huang, G.-L. Li, F. Yang, W. Lin, J.-X. Gu, H.-G. Deng, Z.-G. Gu H.-G. Jin, Donor-Acceptor Mixed-Naphthalene Diimide-Porphyrin MOF for Boosting Photocatalytic Oxidative Coupling of Amines. *ACS Catal.* **2023**, *13*, 5723-5732.

[16] Y.-N. Liu, L.-N. Li, S. Meng, J. Wang, Q. Xu, P.-T. Ma, J.-P. Wang, J.-Y. Niu, Fabrication of Polyoxometalate-Based Metal-Organic Frameworks Integrating Paddlewheel $Rh_2(OAc)_4$ for Visible Light-Driven Oxidative Coupling of Amines. *Inorg. Chem.* **2023**, *62*, 12954-12964.

[17] Shi, J.; Zhang, J.; Liang, T.; Tan, D.; Tan, X.; Wan, Q.; Cheng, X.; Zhang, B.; Han, B.; Liu, L.; Zhang, F.; Chen, G. Bipyridyl-Containing Cadmium-Organic Frameworks for Efficient Photocatalytic Oxidation of Benzylamine. *ACS Appl. Mater. Inter.* **2019**, *11*, 30953-30958.

[18] Y. Zhao, D.-G. Truhlar, Density Functionals with Broad Applicability in Chemistry. *Acc. Chem. Res* **2008**, *41*, 157-167.

[19] T.-H. Dunning Jr, P. J. Hay, Modern Theoretical Chemistry. **1976**.

[20] H. Arı, Z. Büyükmumcu, Comparison of DFT Functionals for Prediction of Band Gap of Conjugated Polymers and Effect of HF Exchange Term Percentage and Basis Set on the Performance. *Com Mater Sci.* **2017**, *138*, 70-76.

[21] Z. Mosapour Kotena, M. Razi, S. Ahmadi, Evaluation of Hydrogen Bonds Formation in the Selected Rare Sugars Based on 6-31G and 6-311* + + G (d, p) Basis Sets. *J. Mol. Model.* **2021**, *27*, 315.

[22] C.-W. Bauschlicher, Basis Set Effects on the Geometry of $C_{96}H_{24}$. *Chem. Phys. Lett.* **2016**, *665*, 100-104.

[23] P.-J. Hay, W.-R. Wadt, Ab Initio Effective Core Potentials for Molecular Calculations. *J. Chem. Phys.* **1985**, *82*, 270.

[24] X. H. Zhang, K. T. Wang, Theoretical Investigation of the Mechanism of Gold(I)-Catalyzed Hydrothiolation of Alkynes and Alkenes with Phenthiol. *Rsc Adv.* **2015**, *5*, 34439-34446.

[25] D.-M. Schmidtt, Holomorphic Chern-Simons Theory and Lambda Models: PCM Case. *J. High.*

Energy. *Phys*. **2020**, *2020*, 60.

[26] M. Saitow, K. Hori, A. Yoshikawa, R. Y. Shimizu, D. Yokogawa, T. Yanai, Multireference Perturbation Theory Combined with PCM and RISM Solvation Models: A Benchmark Study for Chemical Energetics. *J. Phys*. *Chem*. *A*. **2021**, *125*, 8324-8336.

[27] M. P. Andersson, P. Uvdal, New Scale Factors for Harmonic Vibrational Frequencies Using the B3LYP Density Functional Method with the Triple-ζ Basis Set 6-311+G (d, p). *J. Phys*. *Chem*. *A*. **2005**, *109*, 2937-2941.

[28] H.-S. Yu, L. J. Fiedler, I.-M. Alecu, D.-G. Truhlar, Computational Thermochemistry: Automated Generation of Scale Factors for Vibrational Frequencies Calculated by Electronic Structure Model Chemistries. *Comput Phys Commun*. **2017**, *210*,132-138.

[29] Z. Hu, W. Sun, S. Zhu, Chance Constrained Programs with Gaussian Mixture Models. *Iise Trans* **2022**, *54*, 1117-1130.